Journal of Wind Engineering & Industrial Aerodynamics 230 (2022) 105182

Contents lists available at ScienceDirect

Journal of Wind Engineering & Industrial Aerodynamics

journal homepage: www.elsevier.com/locate/jweia

Constant-frequency time cells in the vortex-shedding from a square cylinder in accelerating flows

Stefano Brusco [a,*], Guido Buresti [a], Yuan-Lung Lo [b], Giuseppe Piccardo [a]

[a] Department of Civil, Chemical and Environmental Engineering, DICCA Polytechnic School, University of Genova, Via Montallegro 1, 16145, Genoa, Italy
[b] Department of Civil Engineering, National Taipei University of Technology, Taipei, Taiwan

ARTICLE INFO

Keywords:
Thunderstorm outflows
Transient aerodynamics
Accelerating flows
Wind tunnel tests
Vortex-shedding transient modulation
Constant-frequency time cells

ABSTRACT

An extensive experimental campaign has been carried out in a multiple-fan wind tunnel to study the effects of flow acceleration on a sectional model of a sharp-edged square cylinder. Different levels of positive and negative acceleration are reproduced, which are compatible with those induced by full-scale thunderstorm outflows. Various initial and final conditions are also explored and, in all conditions, multiple test repeats are carried out in order to obtain satisfactory ensemble averages. Particular attention is devoted to the acquisition of signals associated with vortex-shedding, for which tailored time-frequency analyses, based on the continuous wavelet and Hilbert transforms, are introduced. Sensitivity analyses are carried out on a selection of the relevant parameters that better allow the tracing of the temporal variation of the shedding frequency. Time intervals in which the shedding frequency is constant, separated by discontinuities, are found during the transients. The number and extent of such constant-frequency time cells and discontinuities seem to be connected with the flow acceleration, but are not strictly repetitive. For higher levels of acceleration the ensemble mean of the Strouhal number is found to be comparable with or moderately lower than the steady-flow value corresponding to the instantaneous velocity.

1. Introduction

The main source of fluctuating cross-wind forces acting on slender structures is the alternate shedding of vortices in their wakes (e.g., Solari, 1985). Research on this phenomenon, which is typical of bluff bodies, has been carried out for over half a century and the description of its main features has been the subject of several reviews (e.g., Buresti, 1998). The square cross-section is a classic shape with relevance to wind engineering. In fact, during the Seventies, many architects and engineers designed their skyscrapers avoiding any sort of modification of the regular cross-section with height. Consequently, the square cylinder has become a benchmark replicated by many laboratories and research centers to validate their measurements. In particular, numerous investigations were carried out in wind tunnels (e.g., Vickery, 1966; Nakaguchi et al., 1968; Bearman and Trueman, 1972; Ootsuki et al., 1980; Okajima, 1982; Bearman and Obasaju, 1982; Mizota and Okajima, 1982; Obasaju, 1983; Noda and Nakayama, 2003; Dutta et al., 2003; Yang and Mason, 2019). Furthermore, studies have also been performed in water tunnels (e.g., Lyn et al., 1995), or through numerical procedures (e.g., Okajima et al., 1990; Sohankar, 2006). Effects associated with the sharpness of the edges (Tamura and Miyagi, 1999), the presence of free-stream turbulence (Roberson et al., 1972; Lee, 1975; Tamura and Miyagi, 1999; Petty, 1979; Nakamura and Ohya, 1984; Durão et al., 1988; Lyn and Rodi, 1994) and the occurring of Reynolds effects (Norberg, 1993; Chen and Liu, 1999) have also been investigated.

The contribution of these investigations to the design of slender structures in the second part of the last century is fundamental. Indeed, adequate sets of pressure and force coefficients were evaluated for a large range of design configurations. They were subsequently treated as constant quantities and combined with the knowledge of the dynamic pressure in order to derive the full-scale aerodynamic loading, by invoking the applicability of the strip and quasi-steady theory (Kawai, 1983). This procedure is well-consolidated when studying effects on structures induced by synoptic winds, which have steady characteristics in both wind speed and direction (e.g., Solari, 2014; Solari, 2019; Xhelaj et al., 2020). On the other hand, its application might be subverted by the transient nature of thunderstorm outflows. These are non-stationary phenomena occurring at the mesoscale, whose duration may be limited and whose flow direction might exhibit remarkable irregularities (e.g., Holmes et al., 2008; Choi, 2000; De Gaetano et al., 2014). A transient

* Corresponding author.
E-mail address: stefano.brusco@edu.unige.it (S. Brusco).

https://doi.org/10.1016/j.jweia.2022.105182
Received 17 February 2022; Received in revised form 19 September 2022; Accepted 19 September 2022
Available online 5 October 2022

condition is expected to affect the vortex-shedding development and frequency, as well as the pressure and force coefficients, which depend on the regularity and configuration of said vortex-shedding (e.g., Buresti, 2012). Actually, transient aerodynamics constitutes one of the least covered aspects related to thunderstorm outflows (Solari, 2020). Therefore, the applicability of the strip and quasi-steady theory remains questionable.

Contrary to what seen for the steady case, the number of investigations carried out in transient conditions is rather limited. The pioneer of this topic has been Sarpkaya, 1963, 1966, who conducted water tunnel experiments on circular cylinders for impulsively-started flows. Particular attention was given to the variation of the aerodynamic coefficients, which were observed to increase compared to the values found in steady conditions. This line of research was followed by further investigations (Sarpkaya and Kline, 1982; Sarpkaya and Ihrig, 1986), carried out on asymmetric bodies as well as for different flow incidences. In more recent years, because of the growing interest of the Wind Engineering community towards thunderstorm outflows, also traditional wind tunnels have been employed to simulate particular aspects of such phenomena. Chay and Letchford (2002) studied the effects of downbursts on a cube by realizing a stationary wall jet, and the same authors subsequently also reproduced the effects of a translating downburst (Letchford and Chay, 2002). The method of the pulsed wall jet was then developed for the reproduction of the downburst ring vortex (Mason et al., 2005). Shirato et al. (2009) modified their open-circuit suction wind tunnel by installing a shutter placed downstream the wind tunnel model, whose sudden opening would induce a rapid variation of the wind velocity. Then, again, Takeuchi and co-workers (Takeuchi et al., 2008; Takeuchi and Maeda, 2013), studying the aerodynamics of a railcar-like body, reproduced accelerating flows by installing rotating flat-blade rows in the Eiffel type wind tunnel at Kyushu University. The focus of most of these studies concerns the effects of the acceleration on the aerodynamic coefficients. Conversely, less attention has been devoted to the analyses of vortex-shedding in transient conditions. Indeed, to the authors' best knowledge, only Yang and Mason (2019) studied the effects of the acceleration on vortex-shedding and the Strouhal number, considering three different sectional rectangular models. In particular, they focused their attention on the ensemble-averaged Strouhal number evaluated by combining the results from a sufficient number of repeats. Nevertheless, a careful analysis on single experiments still seems to lack in the literature.

In the framework of the ERC Project THUNDERR "*Detection, simulation, modelling and loading of thunderstorm outflows to design wind-safer and cost-efficient structures*" (Solari et al., 2020), the topic of transient aerodynamics is addressed by performing a wind tunnel test campaign at the multiple-fan wind tunnel of the Tamkang University (hereinafter referred to as TKU-MFWT), in Taipei, which has the capability of reproducing flows with positive and negative accelerations. The flexibility of the spatial distribution of the fans might be further exploited to reproduce profiles whose features vary with time, as occurs for thunderstorm outflows (e.g., Lombardo et al., 2014; Gunter and Schroeder, 2015; Canepa et al., 2020). The effects of a sudden change of the wind profile have been preliminary studied at the TKU-MFWT (Mason and Lo, 2019; Lo and Mason, 2019), with focus on the velocity profile: uniform, atmospheric boundary layer and nose-like shape. A further step forward in this topic seems to be represented by the use of artificial intelligence, as proposed by Li et al. (2021).

The present paper aims at investigating the development of the vortex-shedding from a sharp-edged square cylinder subjected to transient flows. In particular, great attention will be devoted to the effects induced on the vortex-shedding frequency, whose variation in the transients is investigated by an appropriate use of time-frequency analyses. This information may be of interest for the prediction of the possible aeroelastic phenomena due to vortex-shedding that may occur during the varying flow conditions typical of thunderstorm outflows. Eventually, comparisons with the reference case represented by the steady flows will be provided.

2. Description of the wind tunnel test campaign

2.1. Experimental facility

The TKU-MFWT (Fig. 1a) is equipped with 72 individually controlled fans to drive the flow, arranged in a 12×6 matrix. The cross section of the test chamber is 1.32 m $\times$ 1.32 m and the remaining dimensions are shown in Fig. 1b, which also includes the location of the test section. No roughness elements are used to develop the velocity profile and all the internal surfaces are smooth. The contraction rate, which is obtained by reducing the vertical dimension only, is 1:2 and the maximum speed is about 16 $\frac{m}{s}$. The turbulence intensity was measured for different wind velocities and its average value was found to be approximately 2.5%, being slightly higher for low levels of wind velocity and lower for higher wind velocities. This value seems consistent with measurements typical of multiple-fan wind tunnels (e.g., Ozono and Ikeda, 2018). The presence of free-stream turbulence is known to interact with the separated shear layers (e.g., Saathoff and Melbourne, 1997), whose mean reattachment length and curvature are modified. This is reflected into a moderate modification of the pressure coefficients and of the shedding frequency, which become a function of the flow properties (i.e., turbulence intensity and integral scale) (Akon and Kopp, 2018; Morrison and Kopp, 2018). Therefore, the outcomes of this wind tunnel test campaign may be somewhat affected by the effects of the free-stream turbulence.

2.2. Wind tunnel model and instrumentation

The wind tunnel model is a sharp-edged square cylinder equipped with 94 pressure taps. The model spans the entire width of the test section (Fig. 1a), which is placed 3.66 m downwind of the entrance to the test chamber (Fig. 1b). The vertical profile of the mean wind speed in correspondence of the model indicates a spatial variation along its axis which increases with the wind speed, reaching discrepancies up to 4–5% from the vertical reference. This variation is higher than the value commonly suggested for traditional general-purpose tunnels (e.g., Barlow et al., 1999). Nonetheless, the variation here highlighted will be considered in the following analyses of results.

The side b of the model cross-section is 6 cm, so that the resultant blockage ratio is less than 5%; its bending frequency has been estimated as 120 Hz, which is adequately above the range of the vortex-shedding frequencies for the present test campaign. The model is studied for zero incidence only (Fig. 2). Out of the 94 pressure taps, 46 are placed in the mid-span section. The distance between the taps is 5 mm, except for the four taps in the upper and lower faces that are 2.5 mm from the leading edges. Three pressure taps have been highlighted with bigger dots. The one denoted as $C06$ is located at the stagnation point of the section, while the signal difference of the couple $C18$ / $C40$ is representative of the vertical load induced by vortex-shedding. The X- and Y- axes are again defined in Fig. 2. Two circular end-plates, whose diameter is 40 cm (almost 7 b) are installed 600 mm apart, leading the model to a slenderness ratio equal to 10 (Fig. 3a).

The instrumentation installed in the wind tunnel has the scope of capturing the pressure and the wind fields generated around the model. Two 64 channels ZOC 33 pressure transducers (Scanivalve Corporation) have been employed, each one incorporating a high speed multiplexer (45 kHz). The sampling frequency is set at 300 Hz, which easily resolves vortex-shedding from the studied configuration. The precision of such instrument is declared as the 0.15% of the full scale (i.e., 2500 Pa), so that the accuracy is $\pm$ 3.75 Pa. All model taps are connected to the corresponding pressure transducer with a 1.5 m PVC tubing, which has an internal diameter of 1.5 mm. Considering the length of the tubes, the raw pressure measurements are treated with the frequency correction technique for both amplitude and phase distortions (Irwin et al., 1979). All the recorded signals are actually differential pressures between those

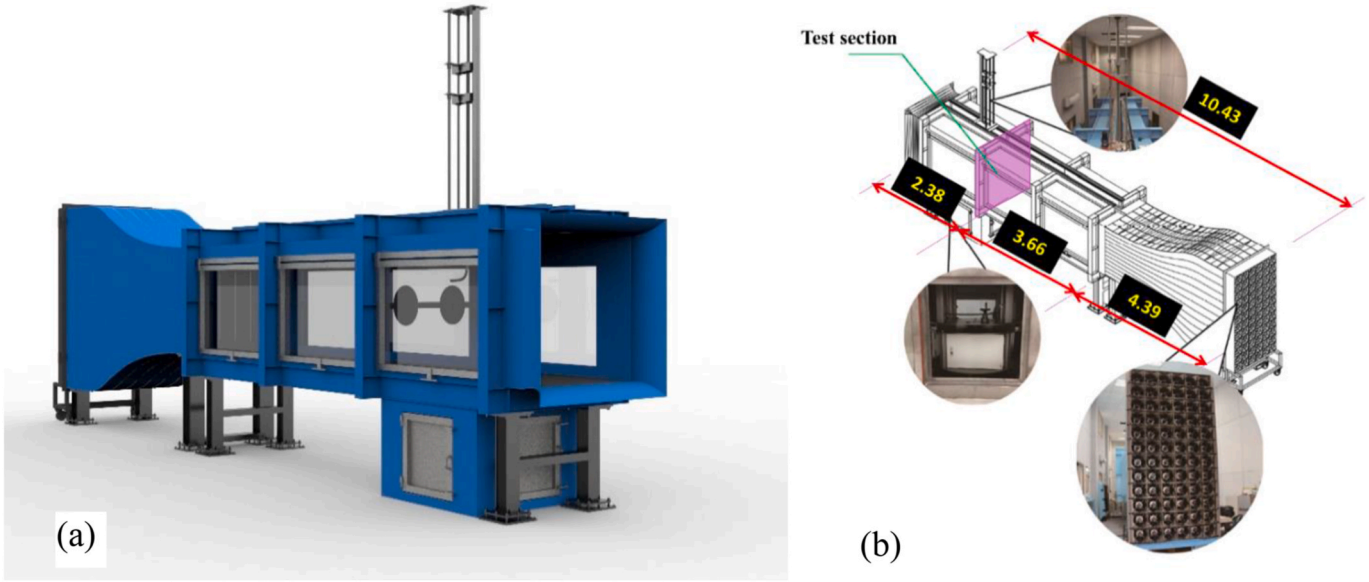

Fig. 1. TKU-MFWT: (a) rendering; (b) 3D view and relevant dimensions.

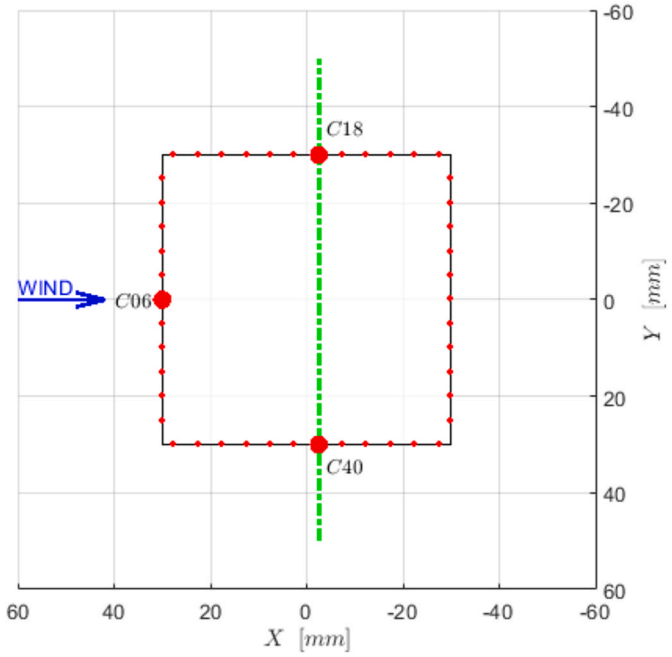

Fig. 2. Tapping scheme of the mid-span section of the sectional model.

acquired at the tap and the reference pressure, which is taken from an adjacent room.

To study the wind field induced around the model, three Pitot-static tubes (hereinafter denoted as $P1$, $P2$ and $P3$) have been used to measure the total and the static pressures and, consequently, the dynamic pressure which acts on the model. In particular, $P2$ and $P3$ are positioned 20 cm above the model axis (Figs. 3a and b), on different sides of the centerline. Both their tips are exactly aligned with the windward face of the model, while $P1$ acquires the total pressure 2 b in front of it (closer to the inlet section). After a thorough analysis of different techniques to estimate the reference dynamic pressure, it was defined as the difference between the pressure recorded by the $C06$ pressure tap and the average mean static pressure recorded by $P2$ and $P3$. This choice has led to a satisfactory level of repeatability and assures a good level of confidence about the simultaneity of the measurements, since the dynamic pressure is sampled with the same acquisition system as the loading data. Moreover, all the three signals derive from the same vertical plane, which is a typical requirement for the study of unsteady flows.

2.3. Flow conditions

The wind tunnel test campaign has been articulated in two different phases. The first involved simulation of steady flows, in which the multiple fan wind tunnel is employed as a traditional facility. Steady flows have been reproduced by setting the reference wind speed U ranging from 4.3 $\frac{m}{s}$ to 15.9 $\frac{m}{s}$. Therefore, the corresponding Reynolds number $Re = \frac{Ub}{\nu}$ (where ν is assumed as $1.5 \times 10^{-5} \frac{m^2}{s}$) covers a range between 1.72×10^4 and 6.34×10^4. In particular, 12 settings have been picked up to define the steady references (hereinafter denoted as SF^1 – SF^{12}, where SF stands for Steady Flows) and at least 25 repeats have been carried out for each of them. Each repeat comprises 2^{16} samples and, thus, it is 218.4 s long.

As far as the simulation of unsteady flows is concerned, a total of 13 different conditions have been simulated, each one characterized by at least 30 repeats. The number of the repeats has been dictated by the need to limit the sources of measurement uncertainty (e.g., Kwan and Kopp, 2021). In contrast to the reproduction of the steady flows, the unsteady cases are characterized by the flow acceleration, which enables the passage from one velocity to another during the transients. Each repeat encloses 2^{16} samples, as for the steady cases.

The baseline test UF_1 (UF = unsteady flow) has been set to feature the maximum absolute values of the acceleration allowed by the TKU-MFWT servomotors. A total of 90 repeats have been conducted for this case, and the signal of the reference velocity of one trial is presented in Fig. 4 (in black). The zooms may aid in better appreciating the positive and negative flow accelerations.

From this time-history, the presence of turbulence in the tunnel is clearly discernible. Moreover, the zooms suggest that the variation of the velocity in the transients is not linear. Consequently, the acceleration cannot be considered as uniform during the ramps. To overcome these issues, a filtering technique based on the continuous wavelet transform was used and will be described in Section 3.2.

In the following, results from selected repeats of UF_1 will be analyzed. The other 12 unsteady conditions have been reproduced by setting different values of the flow parameters, such as the initial and target wind velocities or the flow acceleration in the transients. Amongst

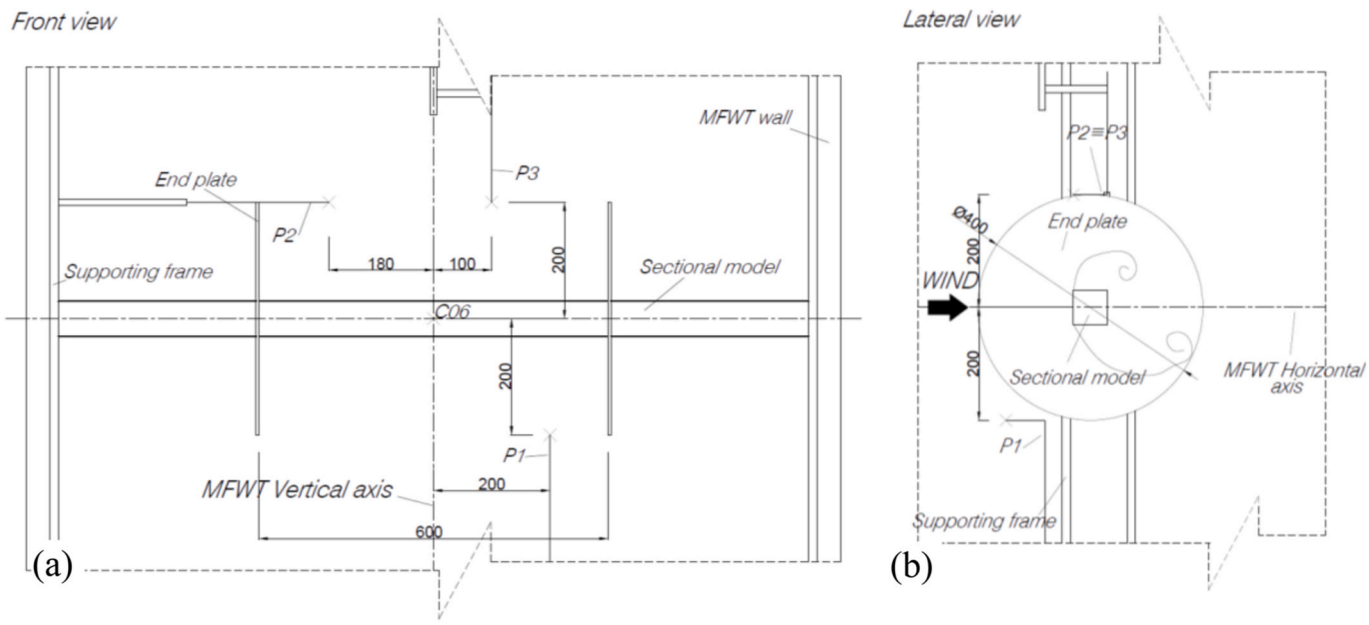

Fig. 3. Wind tunnel model and instrumentations: (a) front view; (b) lateral view.

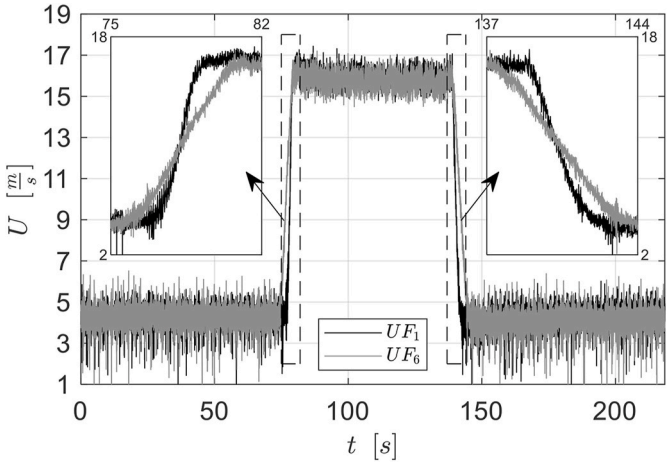

Fig. 4. Comparison between the freestream velocity time histories of single repeats of UF_1 and UF_6.

these, another case of interest is represented by the test UF_6 (Fig. 4, in grey), which differs from UF_1 because of a lower flow acceleration. In this case, 30 repeats have been carried out. For the whole set of unsteady tests, the number of samples and the time length of each time history are the same as in steady conditions. For more details, the reader may refer to the PhD Thesis by Brusco (2021).

3. Methodology

3.1. Time-frequency analyses

Time-frequency analyses are carried out by employing both the continuous wavelet transform and the Hilbert transform (see, e.g., Buresti et al., 2004; Mariotti, 2018).

As for the first one, the complex Morlet wavelet is used, which is defined as follows:

$$\psi(t) = e^{i\omega_0 t} e^{-t^2/2}. \tag{1}$$

The Morlet wavelet is shown to provide an optimal joint time-frequency concentration and furnishes an excellent compromise between time and frequency resolution. Moreover, the user may choose to improve the frequency or the time resolution by simply increasing or decreasing the value of the central frequency ω_0. The output of such transform is a complex time-frequency map, in which various quantities may be displayed. In particular, an important source of information for the analysis of a signal $x(t)$ is represented by the square modulus of the transform, which is directly linked with the energy of the signal and may be analyzed to observe the temporal variation of its dominating harmonic content. Besides, it is possible to integrate in time the values of the square modulus of the wavelet transform to obtain a wavelet power spectrum $P_{x,W}$ (e.g., Mariotti and Buresti, 2013; Mariotti et al., 2017). Furthermore, cross-sections of this map at fixed time approximate a time-varying power spectrum.

Nevertheless, the continuous wavelet transform is not an orthogonal representation and, consequently, it is redundant. This implies that the effects of sudden changes of the dominating frequencies are reflected on the map cross-sections for intervals of time that encompass the instants when the variations occur. This drawback is enhanced if the time resolution worsens, following the adoption of a high value of central frequency ω_0. On the other hand, a higher value of ω_0 translates in a much more refined resolution in the frequency domain. Moreover, it is worth recalling that the map of the square modulus of the wavelet transform may be advantageously used to develop dynamical filters. This is normally accomplished by setting a threshold value and applying it to the energy map of the signal. The values above the threshold are retained by the filter, while those below are put equal to zero. Afterwards, the inverse transform is applied, and the filtered signal can be recovered. This energetic approach is highly convenient when dealing with signals whose dominant frequency is not constant.

The variation of the dominating frequency of a signal may be studied also by the adoption of the Hilbert transform (see, e.g., Buresti et al., 2004; Mariotti, 2018). In particular, the instantaneous frequency $n_{x,H}$ of the signal $x(t)$ may be estimated as:

$$n_{x,H}(t) = \frac{1}{2\pi}\frac{d\phi_x(t)}{dt}, \tag{2}$$

where $\frac{d\phi_x(t)}{dt}$ is the temporal derivative of the phase of the analytical signal associated with $x(t)$. Eq. (2) acquires an important physical meaning if the signal $x(t)$ is asymptotic (i.e., a sinusoidal signal that is

slowly-modulated in amplitude and frequency). If this is the case, $n_{x,H}(t)$ may be considered as the frequency of the sinusoid that best approximates the signal $x(t)$ at each time. If one deals with a signal which is not characterized by a single narrow-band asymptotic component, but dominated by multiple frequencies, each harmonic component has to be separately extracted before carrying out the Hilbert transform. This may be achieved, for instance, by applying the previously described dynamical filter based on the continuous wavelet transform. On the other hand, the same narrow-band filtering procedure is necessary also when a single asymptotic component is present, but it is embedded in noise or, in any case, oscillations at different frequencies are present. Since the instantaneous frequency becomes ill-defined when the modulus of the analytic signal tends to zero, an additional threshold may be applied on the modulus of the analytic signal. The value of this threshold is usually chosen as a suitable percentage of the mean value of the modulus of the analytic signal, which permits to retain at least 50% of the original points (Buresti et al., 2004).

In the following, the continuous wavelet transform and the Hilbert transform will be respectively denoted by CWT and HT.

3.2. Steady flow pressure tests

From each i-th steady flow pressure test, the reference mean wind velocity $\overline{\overline{U}}_i$ ($i = 1$–12), which is the mean value of the mean wind velocity evaluated from each repeat, is obtained. Its values will be singled out in unsteady conditions to allow for comparison between the two conditions.

Analogously, it is possible to evaluate the non-dimensional cross-flow coefficient $c_{\Delta P_L}$ (where the subscript L stands for lift), defined as:

$$c_{\Delta P_L}(t) = \frac{P_{C18}(t) - P_{C40}(t)}{\overline{P}_{dyn}}, \tag{3}$$

where P_{C18} and P_{C40} are the time histories acquired by the pressure taps $C18$ and $C40$ (Fig. 2), and $\overline{P}_{dyn}$ is the mean value of the reference dynamic pressure. For further analyses, the adoption of $c_{\Delta P_L}$, rather than its dimensional counterpart, is strongly convenient in order to study the effects related to unsteady conditions. Should this precaution not be taken, the energy content linked with the higher wind velocity would eclipse any other contribution. $c_{\Delta P_L}$ is representative of the crosswind load and its definition allows precious information to be gathered about vortex-shedding and its frequency. To this end, the time histories of $c_{\Delta P_L}$ are analyzed with the CWT, calibrated on a range between 5.5 and 55.1 Hz (which encompasses the entire harmonic domain of interest for the vortex-shedding) and the central frequency ω_0 is assumed equal to 6π, to enhance the frequency resolution. Besides, the integration in time of the original map may be performed, and the corresponding wavelet power spectrum $P_{c_{\Delta P_L}}$, because of its smoothness, may be employed to easily estimate the Strouhal number S_W (where the subscript W recalls that it is estimated through a wavelet-based procedure), both from a single repeat and from the whole set of steady flow pressure tests SF^1-SF^{12}. The first assessment of the Strouhal number is further refined by carrying out new wavelet analyses on a limited frequency range (2.5 Hz), selected around the original peak in order to better evaluate the frequency corresponding to the maximum in the energy map. The mean value of the Strouhal number for the whole set of tests, $\overline{S}_{W,m}$, is 0.129, oscillating between a minimum of 0.125 and a maximum of 0.132. These values seem in close agreement with the outcomes presented by other researchers in previous studies, already mentioned in the Introduction and described in detail in Table 1. The results in Table 1 were obtained through experiments in wind or water tunnels, apart from the numerical ones by Sohankar (2006), which derive from Large Eddy Simulations (LES). All the values summarized in Table 1, which extend the data furnished by Noda and Nakayama (2003) and Yang and Mason (2019), seem to demonstrate that the Strouhal number estimate is quite robust, being not particularly affected by turbulence or Reynolds number. Actually, the fact that the results of the present experimental campaign are in good agreement with the other values suggests that the non-uniformity of the velocity profile across the wind tunnel did not impact the regular shedding of vortices.

Table 1
List of estimated Strouhal number from previous studies (steady flows). Most of the data have been gathered from Noda and Nakayama (2003) and Yang and Mason (2019).

Author(s)	$\frac{\sqrt{\overline{U^2}}}{\overline{U}}$ [%]	Re	$\overline{S}$
Vickery (1966)	Smooth	10^5	0.118
–	10	–	0.120
Nakaguchi et al., 1968	Smooth	2-6 × 10^4	0.13
Bearman and Trueman (1972)	Smooth	6.8 × 10^4	0.13
Lee (1975)	<0.5	1.76 × 10^4	0.122
–	6.5	1.76 × 10^4	0.126
Ootsuki et al. (1980)	0.2	6.5–7 × 10^4	0.12
Bearman and Obasaju (1982)	Smooth	4.7 × 10^4	0.125
Mizota and Okajima (1982)	Smooth	7.14 × 10^4	0.125
Okajima (1982)	<0.5	4.2 × 10^4	0.13
Obasaju (1983)	<0.04	10^4	0.124
Norberg (1993)	<0.06	5 × 10^3	0.129
–	<0.06	13 × 10^3	0.132
Lyn et al. (1995)	2	2.14 × 10^4	0.132
Chen and Liu (1999)	<0.5	2000–2.1 × 10^4	0.135
Noda and Nakayama (2003)	0.2	6.89 × 10^4	0.131
Dutta et al. (2003)	<0.05	1340–9980	0.141–0.143
Yang and Mason (2019)	<0.5	9300–12.3 × 10^4	0.13
Sohankar (2006)	smooth	2 × 10^4–5 × 10^6	0.13
Present	2.5	1.72–6.34 × 10^4	0.129

On the other hand, the CWT may be advantageously used to develop dynamical filters of a signal, even a non-stationary one (see, e.g., Brusco et al., 2022). This is herein made on $c_{\Delta P_L}$ by imposing a threshold equal to 3 times the mean value of the map. As will be seen in the following Section, this procedure will be consistently applied in the study of the unsteady counterpart of $c_{\Delta P_L}$ to obtain an asymptotic signal, $c_{\Delta P_L,W}$, in order to detect the variation of the instantaneous frequency through the HT.

3.3. Unsteady flow pressure tests

The analysis of repeats associated with steady flows is quite straightforward, since temporal averages are sufficient to define the quantities of interest. A different approach has to be proposed for the analysis of the repeats relevant to the unsteady cases. Firstly, it is necessary to define a time-varying mean wind velocity for each repeat. Its usefulness is driven by the need of an exploring "coordinate" that may identify the actual state of the test, in particular when moving from low to high wind velocity (concerning the ramp-up) and vice versa (concerning the ramp-down). In fact, the original signals (Fig. 4) are inherently affected by turbulence, which makes the time-histories as non-monotonic. From a single repeat of UF_1 (Fig. 4), focus is directed on the portions of the signals relevant to the ramp-up and the ramp-down conditions, which are then isolated and further analyzed. The procedures herein outlined for a single repeat of interest are exported for any repeat of each test carried out under unsteady conditions.

The corresponding time-varying mean dynamic pressure is defined by a dynamical filtering through the CWT, briefly illustrated in Section 3.1, and it is denoted as $P_{dyn,W}$. In this filtering procedure, the frequency domain of interest ranges up to 2.51 Hz, which allows the removal of any sort of influence of the vortex-shedding (whose peak sits on 9.4 Hz for the lowest tested velocity). The central frequency ω_0 is assumed equal to 2π, which usually constitutes the optimal choice for filtering purposes. Hence, the dynamical filter is performed by imposing a threshold equal to 5% of the mean energy. Figs. 5a and b displays the original signals P_{dyn} (in light grey) and their filtered version $P_{dyn,W}$ (in black), together with

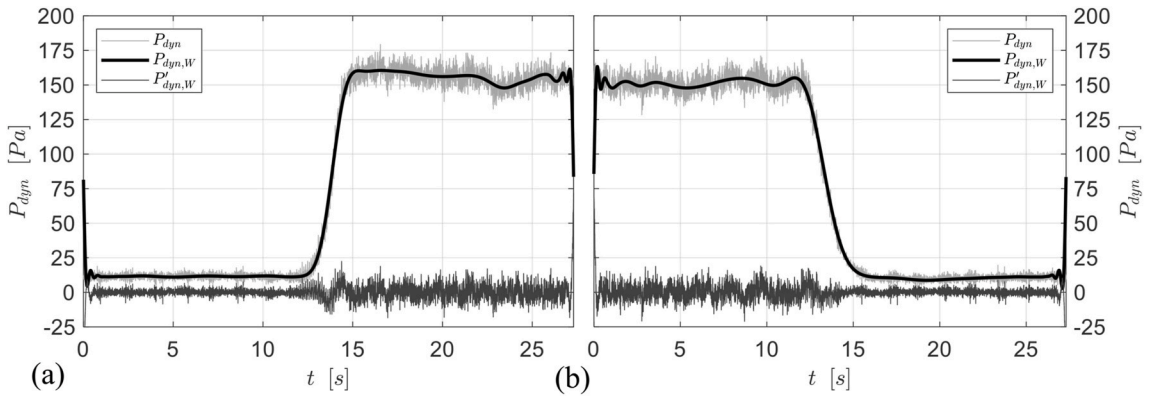

Fig. 5. Filtering of the reference dynamic pressure P_{dyn} for one repeat of UF_1: (a) ramp-up signal; (b) ramp-down signal.

the residual $P'_{dyn,W}$ (in dark grey), for the ramp-up and the ramp-down, respectively. In these pictures, the time axis has been reset and made independent of the originating time history. The evaluation of a time-varying mean wind velocity U_W from $P_{dyn,W}$ is then straightforward.

The definition of a time-varying mean wind velocity U_W is instrumental for the definition of the relevant acceleration, a_W, through a simple numerical derivative. The time histories of a_W (shown in the following) point out that this quantity is not constant during the ramps, but its variation rather resembles a Gaussian curve, for both the ramp-up and ramp-down conditions. For the considered repeat, the maximum acceleration in the ramp-up is estimated as 7.32 $\frac{m}{s^2}$, while in the ramp-down the minimum is equal to -4.93 $\frac{m}{s^2}$. Moving to the elaboration of the 90 repeats of test UF_1, the ensemble means (symbol "$< >$") of the signals relevant to the time-varying mean wind velocities are reported in Figs. 6a and b (ramp-up and ramp-down, respectively), while Figs. 6c and d concern the acceleration. All these signals are reported in black, while the corresponding quantities evaluated from the 30 repeats of test UF_6 (30 repeats) are displayed in grey in the same graphs.

Table 2 lists, from left to right, the maximum and minimum values of the acceleration (ramp-up and ramp-down), and the corresponding mean values in the ramps. These are evaluated by picking the time instants relevant to the beginning and the end of the ramps, identified by imposing $< a>_W = 0.25$ $\frac{m}{s^2}$ (for the beginning and the end of the ramp-up), or $< a>_W = -0.25$ $\frac{m}{s^2}$ (concerning the ramp-down). The subscripts RU and RD refer to ramp-up and ramp-down, respectively.

The numbers associated with a_W may be compared with those typical of full-scale thunderstorm outflows estimated by Brusco et al. (2022). In particular, they analyzed 15 different events, focusing on the acceleration of the slowly-varying mean wind speed, which is therefore

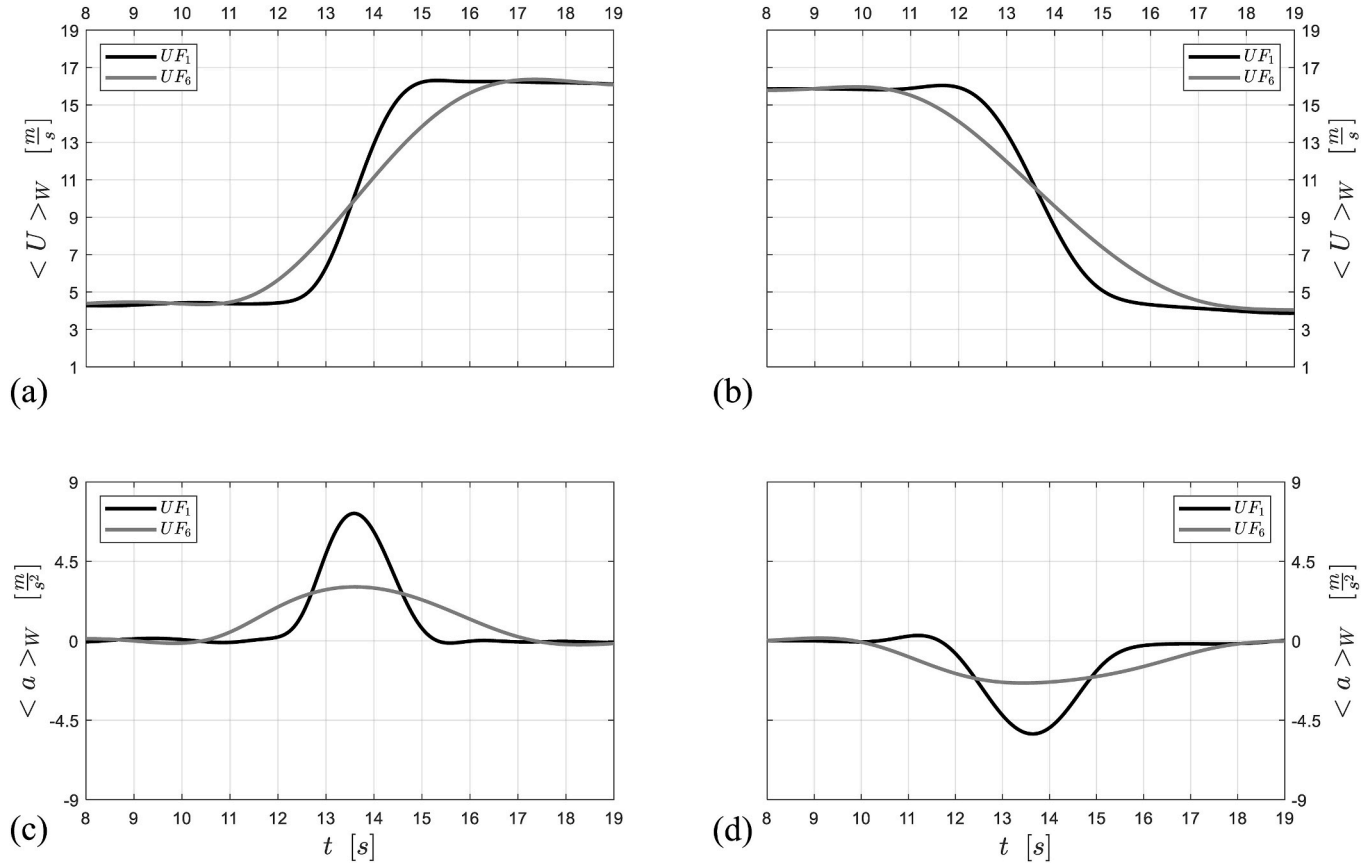

Fig. 6. Ensemble mean carried out on 90 (UF_1) and 30 (UF_6) repeats: (a) ramp-up, U_W; (b) ramp-down, U_W; (c) ramp-up, a_W; (d) ramp-down, a_W.

Table 2
List of characteristics relevant to $< a >_W$ for the accelerating and decelerating flows (ensemble mean).

Name of the test	$< a >_W\|_{RU,max}$ $[\frac{m}{s^2}]$	$< a >_W\|_{RD,min}$ $[\frac{m}{s^2}]$	$\overline{< a >_W}\|_{RU}$ $[\frac{m}{s^2}]$	$\overline{< a >_W}\|_{RD}$ $[\frac{m}{s^2}]$
UF_1	7.21	−5.28	3.80	−2.75
UF_6	3.05	−2.39	1.93	−1.55

associated with components of the energy cascade that may be considered coherent. The maximum value of the acceleration from the set of full-scale events is 1.78 $\frac{m}{s^2}$, while the mean of the 15 maxima is 0.87 $\frac{m}{s^2}$, which is in general lower than those of the current wind tunnel campaign (Table 2). Such discrepancies are mitigated when comparing the time-histories of the ratio between the acceleration and the square value of the wind velocity, $\frac{a_W}{U_W^2}$ (where both numerator and denominator are time-varying quantities). In this case, the same full-scale measurements furnish an estimate of 0.05 $\frac{1}{m}$ as mean of the 15 maxima (being its extreme value equal to 0.18 $\frac{1}{m}$), while this quantity is 0.12 $\frac{1}{m}$ and −0.086 $\frac{1}{m}$ for UF_1 (ramp-up and ramp-down, respectively) and 0.06 $\frac{1}{m}$ and −0.046 $\frac{1}{m}$ for UF_6. These last numbers may be easily converted to the non-dimensional acceleration parameter $K_{a,W} = \frac{a_W}{U_W^2} b$, whose values lie in a range from 0.007 to −0.005 for UF_1, and from 0.0036 to −0.003 for UF_6. Given these sets of numbers, it seems possible to satisfy the similarity of the acceleration parameter $K_{a,W}$. Indeed, if one considers the values found in the full-scale events for the ratio between the acceleration and the square value of the wind velocity, the experiments herein described might be representative of the effects induced by a real thunderstorm outflow on a two-dimensional square element having equal (for UF_6) or slightly greater (e.g., double, for UF_1) dimensions of the model tested at TKU-MFWT. On the other hand, square elements/structures characterized by larger dimensions might still be represented by this wind tunnel test campaign by accepting that the reproduced ratio between the acceleration and the square value of the wind velocity would be lower than the aforesaid extreme values of the full-scale events.

It is now possible to introduce the unsteady counterpart of the non-dimensional cross-flow coefficient (defined for steady conditions by Eq. (3)):

$$c_{\Delta P_L}(t) = \frac{P_{C18}(t) - P_{C40}(t)}{P_{dyn,W}(t)}. \tag{4}$$

Retracing the same steps followed for P_{dyn}, the portions of the signal $c_{\Delta P_L}$ linked with the ramps are extracted and isolated. Figs. 7a–d and 8a-d report time-histories of quantities related to the ramp-up and to the ramp-down conditions, respectively. Figs. 7a and 8a display the variation of the wind velocity, while the relevant accelerations are presented in Figs. 7b and 8b. Figs. 7c and 8c concern the non-dimensional cross-flow coefficient $c_{\Delta P_L}$, in black, being overlapped by $c_{\Delta P_L,W}$, in grey, which is the component of $c_{\Delta P_L}$ strictly linked with vortex-shedding. $c_{\Delta P_L,W}$ is an asymptotic signal (thus, a suitable candidate to undergo the HT) and is obtained by adopting the dynamical filter illustrated for steady conditions in Section 3.2 as regards $c_{\Delta P_L}$, which is now applied on its unsteady counterpart in order to remove the effects linked with turbulence and maintain the energy associated with the time-varying vortex-shedding peak. Hence, Figs. 7d and 8d report the energy map of $c_{\Delta P_L}$, evaluated through the CWT by adopting the same parameters of the steady cases (again, Section 3.2), namely by assuming $\omega_0 = 6\pi$ and a threshold equal to 3 times the mean value of the map. Sensitivity tests on the choice of ω_0 (specifically, 2π and 4π) are presented in Brusco (2021), and their outcomes will be discussed in the following, as well as the justification of using $\omega_0 = 6\pi$. In all the pictures, the time axis is set to focus on the changes of the wind velocity, being extended for just 3.2 s in the ramp-up case, and for 4 s in the descending phase.

The time-histories of $c_{\Delta P_L}$ immediately reveal that the variation of the shedding frequency is not always regular. The passage from one condition to another seems to occur either with a regular pattern or through phases in which the frequency is quite constant, interspersed by abrupt changes. These are characterized by a sudden decrease of the signal amplitude. This unveils a local violation of the Strouhal law, as the shedding frequency does not vary with the same rate as the velocity. Moreover, in the middle of the ramps (i.e., where the acceleration achieves a maximum), a reduction of the energy is seen in Figs. 7d and 8d. In particular, the ramp-up case seems to exhibit larger reduced-energy areas than the ramp-down. This lack of energy associated with specific time intervals indicates a possible weakening of vortex-shedding. The comparison between the energy maps evaluated through the different Morlet bases (see Brusco, 2021) highlights that a higher value of the central frequency best clarifies the presence of discontinuities. In particular, they are localized in correspondence of a mitigation of the signal amplitude, which separates parts of the signals characterized by different shedding frequencies, clearly detectable also from a visual inspection of the signal. In particular, the choice of a central frequency $\omega_0 = 6\pi$ appears to be the one which best exalts this effect, successfully capturing the different regimes of the signal and clearly identifying the changes in frequency, thus pointing out the local violation of the Strouhal law.

Graphs that are similar to those shown in Figs. 7a-d and 8a-d are presented in Brusco (2021) for different repeats of UF_1 and UF_6, as well as for different values of ω_0 and for tests characterized by different values of initial and target wind velocity.

4. Results

4.1. Ridges from a single repeat

The time-frequency analyses of the repeat of interest introduced in Section 3.3 are again considered, now with the aim of extracting the relevant ridges. As far as the CWT is concerned, a ridge has been assumed to coincide with the line that links all the instantaneous maxima of the energy map. On the other hand, for the HT applied on $c_{\Delta P_L,W}$, the ridges may be directly obtained by using Eq. (2).

Starting with the results from the CWT, Fig. 9a shows the relevant ridges $n_{c_{\Delta P_L,W}}$ for the ramp-up condition, evaluated through three different levels of ω_0. These are all drawn with continuous lines and distinguished by adopting a different scale of grey. On the other hand, the black dash-dotted line provides the theoretical variation of the frequency following the Strouhal frequency-velocity law, according to a quasi-steady formulation ("QS" in the legend). This is evaluated by using U_W and a corresponding mean value of the Strouhal number, derived from the steady flow tests. Finally, the black dots indicate the estimate of the instantaneous frequency dictated by the temporal spacing between the maxima of $c_{\Delta P_L,W}$. This procedure, although apparently unsophisticated, is supposed to be less affected by the future or the past of the signal, contrary to what happens with the CWT, especially if its central frequency is high. The presence of a few spurious black points is visible, and these are often linked to a low amplitude of $c_{\Delta P_L,W}$. Fig. 9b displays the same black dots and the black dash-dotted line mentioned before, this time overlapped by the ridge evaluated with the HT applied on $c_{\Delta P_L,W}$. In doing so, the instantaneous frequency is evaluated by setting a threshold equal to the 50% of the mean value of the absolute value of its analytic signal. Tests with thresholds of 25% and 40% have been carried

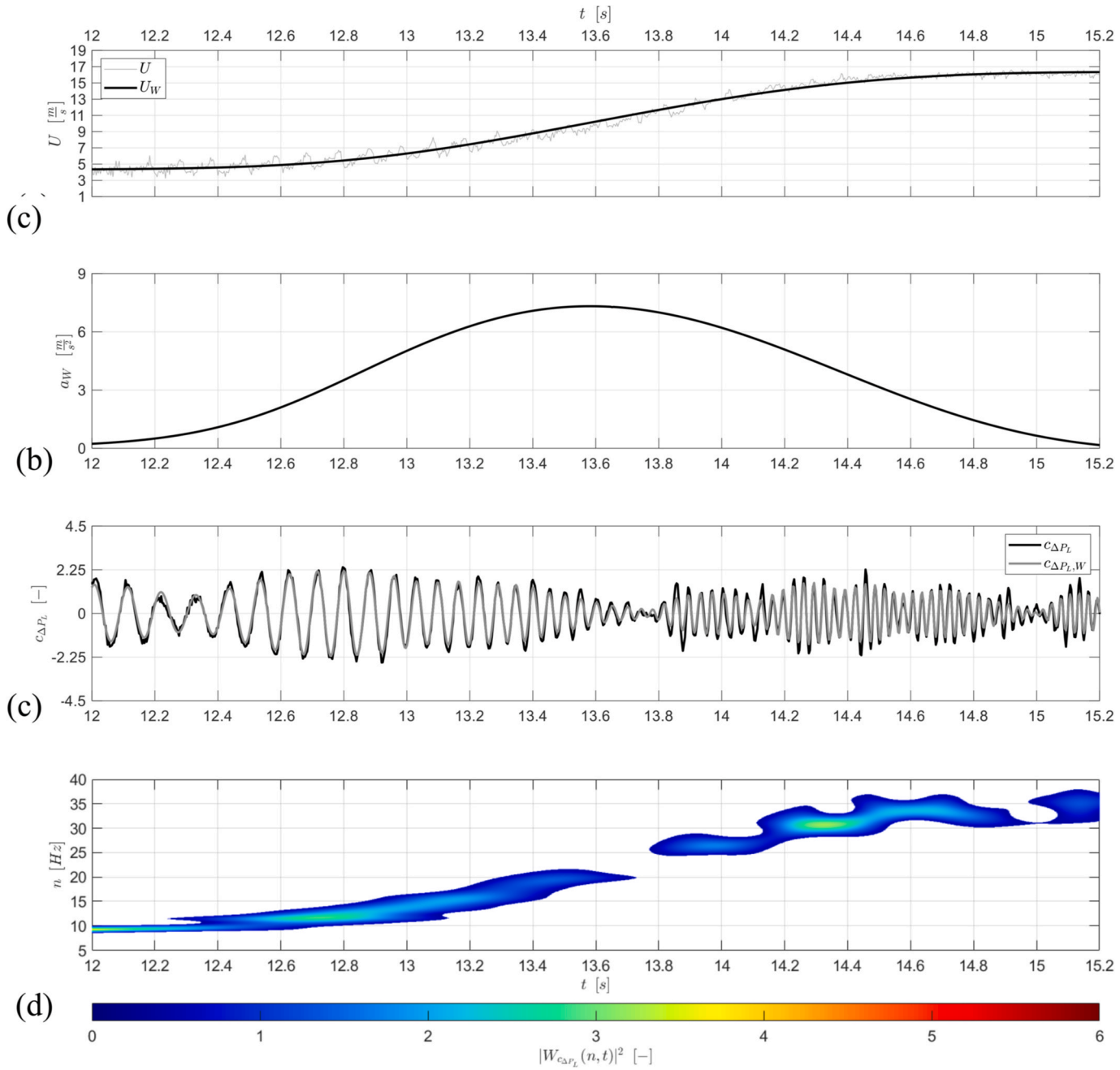

Fig. 7. Signals of simultaneous quantities, focusing on a ramp-up repeat of UF_1: (a) U, U_W; (b) a_W; (c) $c_{\Delta P_L}$ and $c_{\Delta P_L,W}$; (d) $\left|W_{c_{\Delta P_L}}\right|^2$, $\omega_0 = 6\pi$.

out as well, but the choice of a higher filter is the one that provides the clearest trend. Analogously to Figs. 9a and b for the ramp-up case, Figs. 10a and b focus on the ramp-down condition.

Analyzing Figs. 9a and 10a, the extracted ridges appear to be less oscillating when evaluated with a higher level of central frequency, thus better highlighting the discrete change in the shedding frequency. Therefore, it may be expedient to choose a high value of ω_0 (as in Figs. 7d and 8d) since, by virtue of its higher resolution in frequency, it may better capture what could already be visually observed in the time histories of Section 3.3. Moreover, their comparisons with the direct estimates of the instantaneous frequency (black dots in Figs. 9a, b, 10a and 10b) appear to be sufficiently consistent, being satisfactory for lower levels of acceleration, particularly at low wind speed. In contrast, the analysis for low acceleration but at high velocity seems to be affected by some discrepancies. However, the entire set of techniques is seen to clearly capture the discrete jumps, which are particularly evident for $t \sim$ 13.8 s (for both the ramp-up and ramp-down conditions). This time instant seems also to be highlighted from a local drop of energy in the maps (Figs. 7d and 8d). Concerning the analysis of the ridges from the Hilbert transform, $n_{c_{\Delta P_L},H}$ (Figs. 9b and 10b), their oscillations resemble the case of CWT with $\omega_0 = 2\pi$. The discontinuities are not so clear as in the case of CWT with $\omega_0 = 6\pi$, but still suggest a discrete change of the frequency corresponding to local reductions of the amplitude of $c_{\Delta P_L,W}$.

The presence of the discontinuities may also be highlighted by the analysis of the trends of the time-varying Strouhal number in unsteady conditions S_W, which can be evaluated as follows:

$$S_W(t) = \frac{n_{c_{\Delta P_L}}(t)}{U_W(t)} b, \tag{5}$$

where $n_{c_{\Delta P_L}}$ is the frequency from the ridge of the signal, evaluated with one of the methods illustrated before. For instance, adopting the ridges

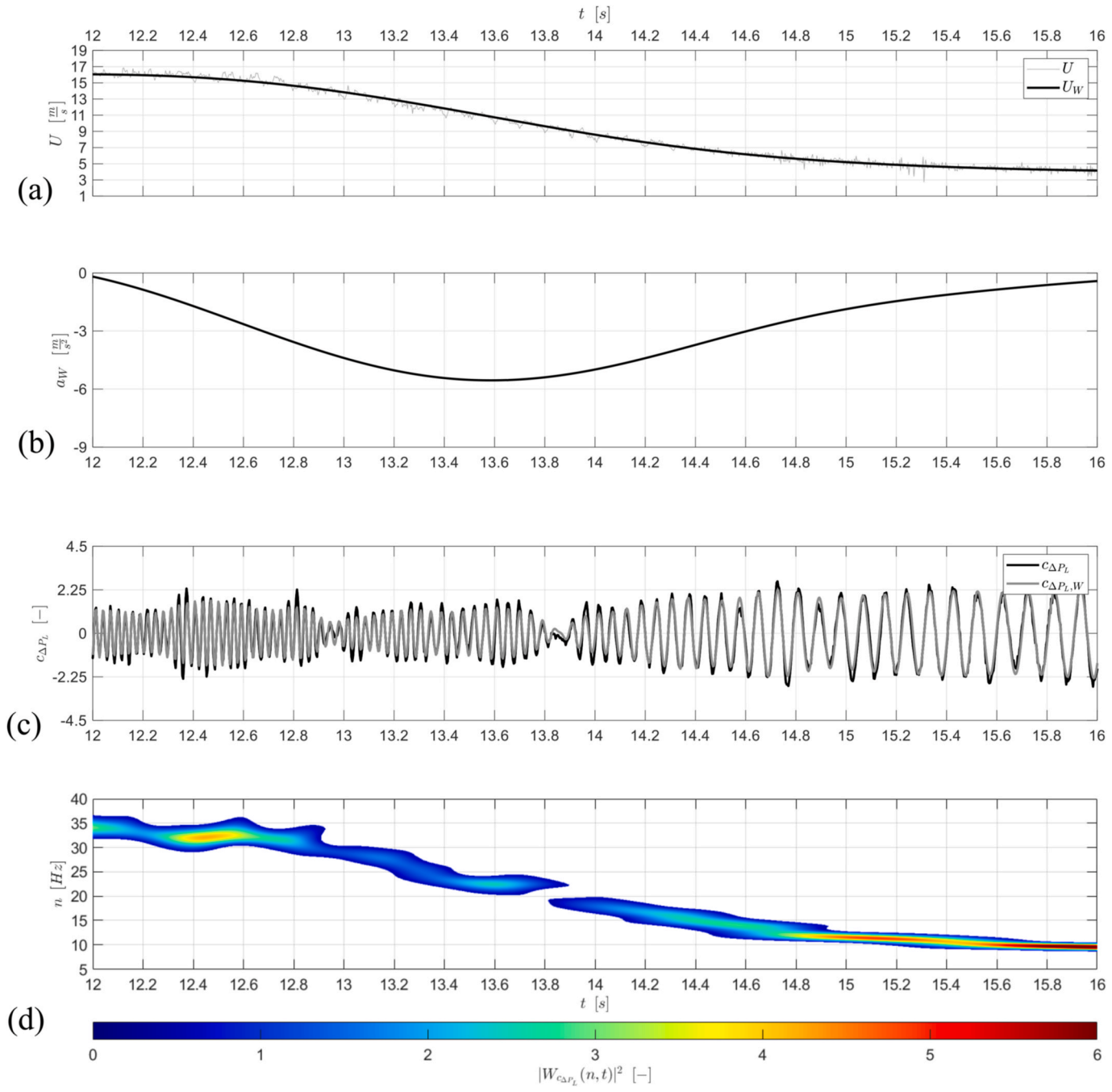

Fig. 8. Signals of simultaneous quantities, focusing on a ramp-down repeat of UF_1: (a) U, U_W; (b) a_W; (c) $c_{\Delta P_L}$ and $c_{\Delta P_L,W}$; (d) $\left|W_{c_{\Delta P_L}}\right|^2$, $\omega_0 = 6\pi$.

evaluated with the CWT using a central frequency $\omega_0 = 6\pi$, it is possible to draw the black lines in Figs. 11a and b (ramp-up and ramp-down, respectively).

The abrupt changes found on S_W confirm the previous findings concerning the discontinuity in frequency, pointing out a clear violation of the theoretical Strouhal law. By comparing the two conditions (ramp-up and ramp-down), their trends appear different. Indeed, during the time intervals in which the frequency remains constant (constant-frequency time cells), the Strouhal number decreases in the ramp-up, while the opposite occurs in the ramp-down. The discontinuities clearly display the passage from one constant-frequency cell to another one or to a condition in which the shedding frequency approximately follows the variation of velocity, and thus the Strouhal number is nearly constant.

The conclusion that may be drawn from the analysis of these results is that in presence of an accelerating flow the vortex-shedding frequency does not always follow linearly the variation of the wind speed. Furthermore, from a careful analysis of all the repeats and conditions considered in the present campaign, it is possible to observe that the number of constant-frequency cells, as well as the timing of their occurrence, are not completely regular. In fact, while it seems possible to appreciate that many of them occur in correspondence of or immediately after high absolute values of the acceleration, the instants or the values of the acceleration corresponding to these events seem to differ from case to case. This might be due to the effect of the relatively high level of free-stream turbulence, which may cause instantaneous velocities that differ from those of the reference filtered transient.

Nonetheless, it is possible to find a recursive trend between the

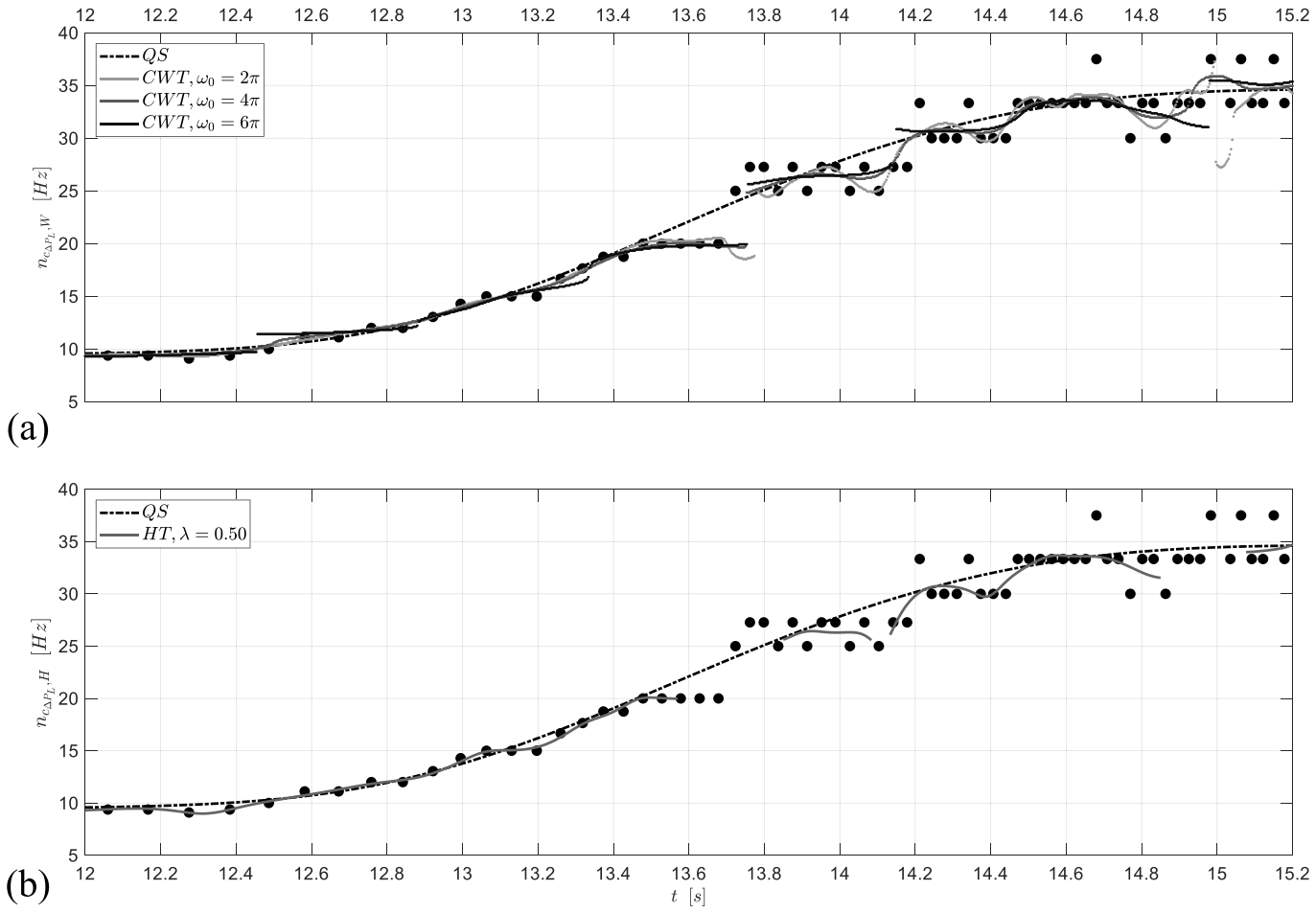

Fig. 9. Ridges of $c_{\Delta P_L}$, focusing on a ramp-up repeat of UF_1: (a) CWT; (b) HT ($c_{\Delta P_L,W}$).

ridges and the Strouhal theoretical curve. Indeed, all the ridges always appear to remain at frequencies that are lower than the reference steady ones. Finally, it is worth noting that the difference between steady and transient vortex-shedding is found to be more pronounced for the ramp-up rather than for the ramp-down conditions. This outcome might be due to the higher magnitude of the absolute values of the acceleration in the ramp-ups. On the other hand, the discrepancies between the two conditions have been seen to be mitigated when the initial (for the ramp-up) or target (ramp-down) wind velocity increases, even with different maxima of the absolute value of the acceleration in ramp-up and ramp-down conditions (Brusco, 2021). In any case, it is reasonable to suppose that the sign of the acceleration might have an influence in producing different wake patterns, possibly related to different dynamics of the shedding vortices in the two conditions.

A further analysis will now be carried out to highlight the instantaneous power spectrum of the signal at the time instants (τ) corresponding to the frequency discontinuities. To this end, the CWT with $\omega_0 = 6\pi$ is employed as the main technique to analyze $c_{\Delta P_L}$. In doing so, the following Figs. 12 and 13 are composed of five sub-plots (1)–(5). In particular, (1) shows the time-history of U and U_W, while (2) and (3) follow the evolution of a_W and $c_{\Delta P_L}$. In each of these time-histories, two vertical lines are indicated. They correspond to the temporal instants to which the cross-section of the map $\left|W_{c_{\Delta P_L}}(n, t=\tau)\right|^2$ refers to in sub-plots (4) and (5). These two last figures also provide, in the lower part of the graphs, the numeric quantification of U_W and a_W for the selected instant τ. Moreover, the peak frequency $n_{VS,W}$ is indicated with a black dot and its estimate is reported. Focus is now given on the ramp-up, precisely on one of the discontinuities pointed out by Fig. 9a ($\tau \sim 13.8$ s). This shift in the frequency appears to be captured also from a visual inspection: the black dots in Fig. 9a and b estimate the instantaneous frequency to be locked on ~ 20 Hz ($\tau < 13.8$ s), before abruptly swapping to ~ 25.7 Hz ($\tau > 13.8$ s). During the transition, the oscillations of the signal seem to be strongly lowered (see sub-plot (3)). The temporal location of the picked instants τ encompassing the discontinuity is provided in the figure caption.

By the combined analysis of Fig. 12-(4) and Fig. 12-(5), the discrete change of the shedding frequency stands out very clearly, confirming the results of the analysis on the ridges. This appears to be reflected by the presence in Fig. 12-(4) of the peak sitting at 19.9 Hz, already present in the previous instants, but whose magnitude is continuously decreasing. Moreover, a large area is building up between $\sim$ 23 Hz and $\sim$ 30 Hz, which exhibits a peak at 25.7 Hz in Fig. 12-(5), where this new peak has become higher than the previous one. This change occurs immediately after the reaching of the maximum acceleration, and thus at the beginning of the descending phase of a_W. In both figures two peaks are found and indeed the presence of double-peaked spectra, whose magnitudes increase and decrease with time, points out the occurrence of a discrete change of frequency. This finding appears to be fully pointed out if a video-animation is played, reporting the simultaneous variations of the quantities indicated in Fig. 12 (such file is provided in the supplementary material, see Appendix A).

This allows a justification of what already pointed out in Section 3.3, where the ridge has been defined by picking the instantaneous maximum of the energy map. This choice might be considered questionable, since it completely neglects the possible significance of the presence of two simultaneous peaks, by excluding the lower-energy one.

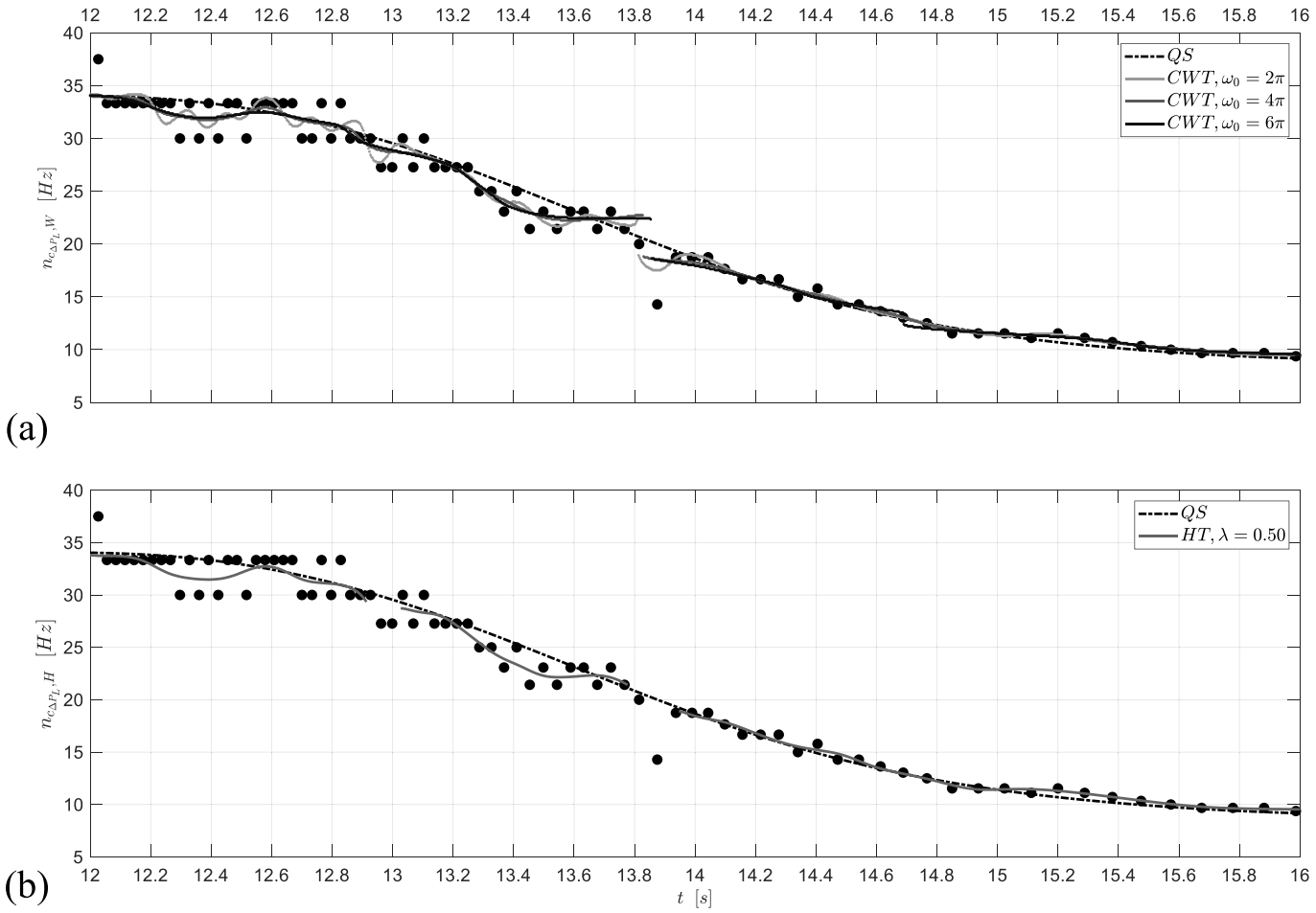

Fig. 10. Ridges of $c_{\Delta P_L}$, focusing on a ramp-down repeat of UF_1: (a) CWT; (b) HT ($c_{\Delta P_L,W}$).

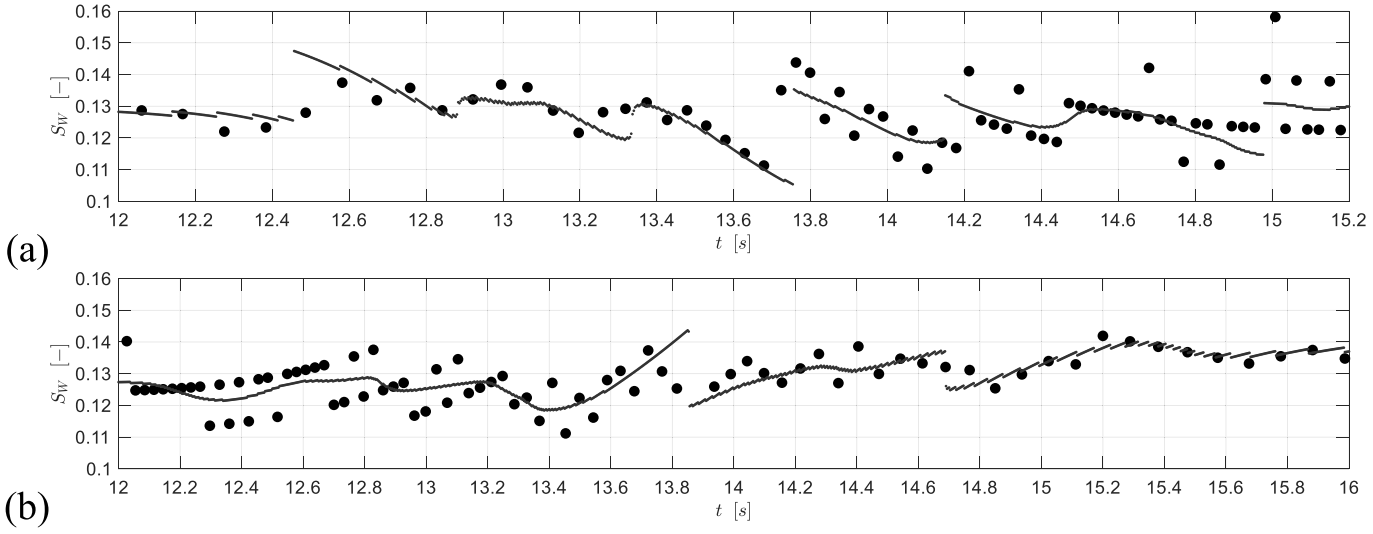

Fig. 11. Time-varying Strouhal number in unsteady conditions S_W: (a) ramp-up; (b) ramp-down.

Nonetheless, the adoption of a high ω_0 aids in stressing the discrete change of frequency, whose presence has been revealed by the Hilbert analyses as well. Indeed, a weak resolution in time exacerbates the effects exerted by past and future states on the actual one, highlighting the presence of simultaneous peaks in the instantaneous cross-sections of the energy map.

Analogously to Fig. 12, Fig. 13 displays two cross-sections of the energy map for the ramp-down case. The two selected time instants again encompass the discontinuity happening at $\tau \sim 13.8$ s. As may be appreciated from the time history of $c_{\Delta P_L}$ (sub-plots (3)), in its correspondence there is a stretch of the signal characterized by mitigated oscillations. Figs. 13-(4) and (5) again reveal the presence of double-

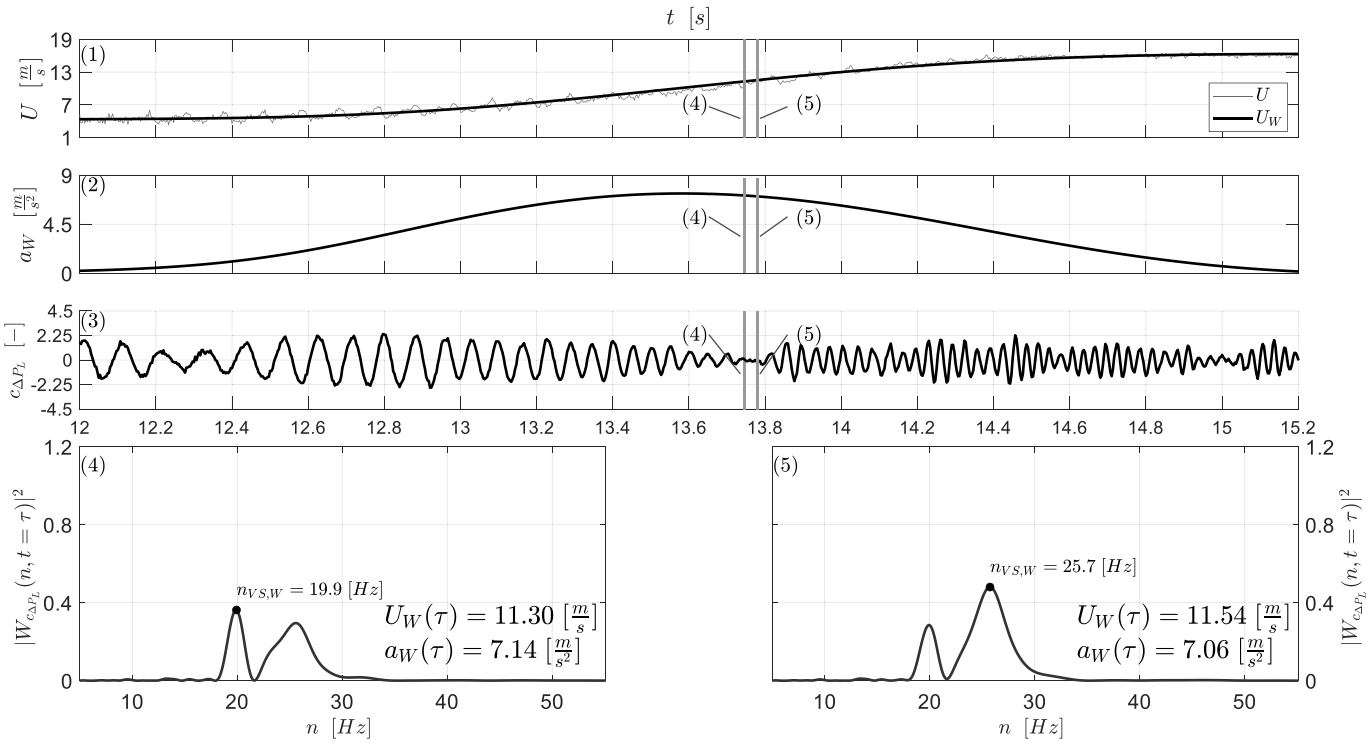

Fig. 12. Cross-sections of $\left|W_{c_{\Delta P_L},U}\right|^2$ for different time instants τ focusing on a ramp-up repeat of UF_1. The sub-plots refer to: (1) U, U_W; (2) a_W; (3) $c_{\Delta P_L}$; (4) $\left|W_{c_{\Delta P_L}}(n, t = 13.75\,s)\right|^2$; (5) $\left|W_{c_{\Delta P_L}}(n, t = 13.78\,s)\right|^2$.

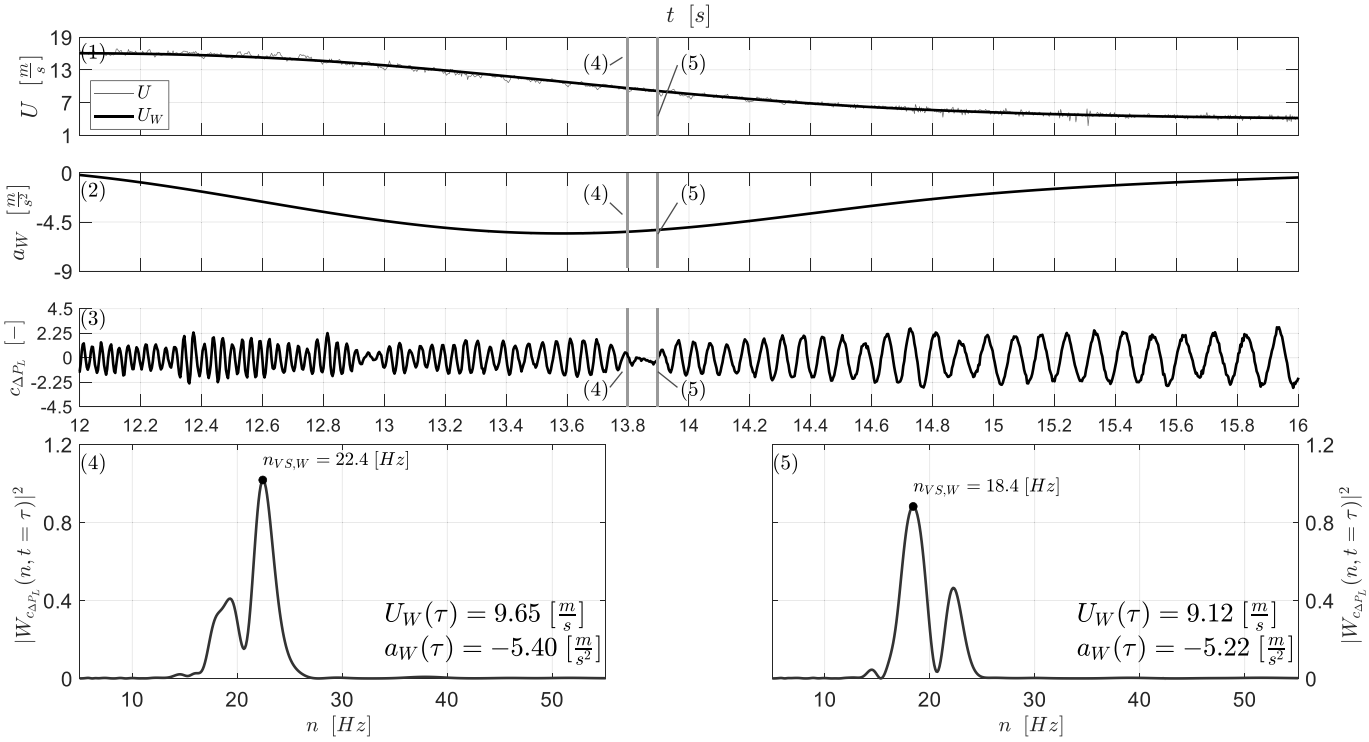

Fig. 13. Cross-sections of $\left|W_{c_{\Delta P_L},U}\right|^2$ for different time instants τ focusing on a ramp-down repeat of UF_1. The sub-plots refer to: (1) U, U_W; (2) a_W; (3) $c_{\Delta P_L}$; (4) $\left|W_{c_{\Delta P_L}}(n, t = 13.80\,s)\right|^2$; (5) $\left|W_{c_{\Delta P_L}}(n, t = 13.90\,s)\right|^2$.

peaked spectra. Now the shift is estimated to move from 22.4 Hz to 18.4 Hz. This discrete change occurs while the acceleration has just achieved a minimum, in perfect equivalence to what registered in the ramp-up case.

Concerning the ramp-up, other discontinuities were registered besides the one shown in Fig. 12, namely for $\tau = 12.45\,s$ (shift from 9.7 to 11.4 Hz), $\tau = 14.15\,s$ (from 27.6 to 30.8 Hz) and $\tau = 14.98\,s$ (from 31.1 to 35.5 Hz). Moving to the ramp-down (Fig. 13), only one another

discontinuity was found, occurring for $\tau = 14.69\,s$ (drop from 13.5 to 12.4 Hz). The relevant pictures are presented in the PhD Thesis by Brusco (2021).

Up to this point, much attention was devoted to the presence of discontinuities; however, it should also be noted that the variation of the frequency appears to be quite regular for a significant portion of the time-interval of the ramp, particularly when the acceleration is low. This is testified by the continuous trends often expressed by the ridges of the signals analyzed earlier.

4.2. Effect of the acceleration on the ridges

Attention is now extended to one repeat of the test UF_6, which has a lower value of the acceleration compared to UF_1; in terms of maximum accelerations, these are in the order of 40% of the UF_1 values. The relevant ridges (displayed by Brusco, 2021) still appear to be below the theoretical curve associated with the steady-state Strouhal number.

To further understand the role of the acceleration, it is possible to count and to quantify the discontinuities exhibited by the ridges, by collecting the values of a_W corresponding to their occurrences. This is shown in Fig. 14, which entails the result for three different repeats of each test UF_1 and UF_6 (taking both ramp-up and ramp-down conditions into account). The ordinate displays the discrete estimated jump in frequency (evaluated as the difference between the frequencies of the ridge at the discontinuity). Only values greater than 1 Hz (in modulus) have been considered in this analysis. Fig. 14 also reveals the presence of a point in the ramp-up conditions which seems slightly out of the prevailing trend of the figure, and which is due to a discontinuity occurring at the end of the ramp-up ($\tau = 14.98\,s$) of the repeat of UF_1.

The connection between flow acceleration and emergence of discontinuities in the vortex-shedding frequency (in terms of both number and magnitude) is pointed out by Fig. 14, which also shows that a higher number of discontinuities is present in the ramp-up rather than in the ramp-down. Moreover, other results (not reported in this paper for the sake of brevity) confirm this behavior for different sets of tests, carried out with different levels of acceleration and linked by the same values of initial and target wind velocity. In particular, when the initial wind velocity is higher (and so is the initial Reynolds number), the trend becomes even clearer.

To stress even more the role played by the acceleration, it seems possible to draw the variation of the ridges no longer along the temporal axis, but rather against the quantity a_W. Fig. 15 reports such variations of the ridges (by setting $\omega_0 = 6\pi$) for the cases selected from UF_1 and UF_6. This choice allows a comprehensive view of the whole process, taking both ramp-up and ramp-down conditions into account at the same time (i.e., ramp-up on the positive abscissa and ramp-down on the negative one). The time-history of the ridges may be followed by moving anticlockwise, starting from almost null values of a_W, reaching their maximum absolute values (ramp-up) and then descending (ramp-down). The role of the acceleration clearly stands out, being the lines associated with UF_1 much more discontinuous than the one relevant to UF_6, whose transition between the same frequencies is more regular, albeit not straightforward.

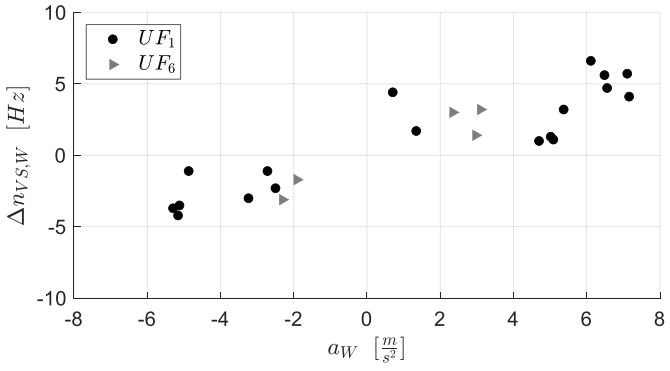

Fig. 14. Estimation of the frequency discontinuity magnitudes from three repeats of UF_1 and UF_6, as a function of the associated value of a_W.

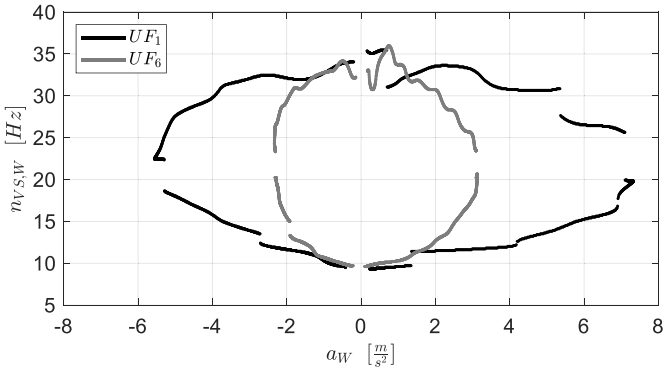

Fig. 15. Variation of the ridges from repeats of UF_1 and UF_6 with a_W.

The pattern of the variation of the shedding frequency with time in presence of an accelerating upstream flow recalls another remarkable phenomenon in bluff-body aerodynamics, namely the vortex-shedding from a two-dimensional body immersed in a flow whose velocity is not constant along the axis. This is a typical situation in Structural Engineering, associated with the wind boundary layer acting on slender vertical structures (e.g., Buresti, 1998). In that case, the velocity variation induces a three-dimensional effect on the vortex-shedding, which occurs in spanwise cells. These are areas characterized by a constant shedding frequency (Maull and Young, 1973). Therefore, discrete changes of frequency are detectable when moving along the model axis. Over the years, many researchers have investigated this phenomenon, studying in particular the number and the span of the cells (Mair and Stansby, 1975), and arrived at the definition of a ruling shear parameter, which is a function of the spanwise velocity gradient, the dimension of the body and the upstream velocity at the centerline of the body. In light of these remarks, it seems possible to find analogies with the analysis of vortex-shedding in transient conditions. Indeed, the effect of the acceleration generates discontinuities of the shedding frequency, now along the time axis, rather than along the spatial axis. In this case, it seems challenging to define the ruling parameter which dictates the number of discontinuities and their magnitudes. However, from all the previous analyses and considerations, it seems clear that it should be connected with the flow acceleration. The higher the acceleration, the higher the number of constant-frequency time cells and the magnitudes of the associated discrete changes in frequency, which is a local violation of the theoretical Strouhal law. The analogy between shear and transient flow conditions is testified by a striking statement made in the pioneering work by Vickery and Clark (1972). Commenting on the results of the variation of the shedding frequency along the height of a tapered cylinder subjected to an uniform flow (a situation which, to a degree, is analogous to a shear flow acting on a non-tapering cylinder), they wrote: " … *While there is a tendency for the shedding frequency to shift in accordance with a constant local Strouhal number, there are regions of substantial length over which no variation takes place. Double-peaked spectra were observed at a number of positions* … ". Double-peaked spectra have indeed been found also in the present work when analyzing the signals of $c_{\Delta P_L}$ in transient conditions, now detected through the time-variation of the instantaneous cross-sections of the relevant energy map.

4.3. Analysis of the ensemble means

In the previous Section attention was given to the irregularities in the shedding frequency found during the transients when studying selected repeats. In order to try to discern an average trend, the whole set of repeats of the test UF_1 is now considered. In particular, each of the 90

repeats is explored by following the time variation of U_W. When this quantity equals one of the corresponding reference mean wind speeds ($U_W = \overline{\overline{U}}_i$, i = 2–11) evaluated in steady conditions (Section 3.2), the relevant cross-section of the wavelet map is examined. This instantaneous wavelet power spectrum is employed to estimate the instantaneous shedding frequency $n_{VS,W}$ for each of the reference velocities, as well as the instantaneous values of the acceleration a_W. Subsequently, the ensemble mean of the instantaneous shedding frequency for each reference value may be evaluated. Moreover, an estimate of the accuracy of the measurements may be provided through the standard deviation of the random variable $n_{VS,W}$, divided by the square root of the number of repeats. Finally, the shedding frequencies in the unsteady cases may be compared with their steady counterparts for each of the ten reference values. Fig. 16 summarizes this comparison, by reporting in the ordinate the ratio between the shedding frequencies in unsteady (evaluated through an ensemble mean) and steady conditions. It is worth noting that, because of the definition of the time-varying Strouhal number, Eq. (5), this ratio coincides with the comparison between the Strouhal number in unsteady and steady conditions. The abscissa refers to the ensemble mean of the acceleration and the black unitary dashed line expresses the steady-case reference. Ten black points are presented in each semi-abscissa axis, surrounded by the corresponding error bars, which indicate the relevant accuracy of the measurement, i.e. twice the standard deviation of the distribution. The ten points of each branch are linked through a black line providing them with their temporal order, which is also suggested by the presence of small arrows. Starting with the ramp-up, when the acceleration increases the curve bends, moving to lower values of the ordinate, before recovering once the ramp-up is approaching its end and the acceleration decreases. Overall, the ramp-down exhibits a similar behavior, although not as neat as in the ramp-up case.

Therefore, the trend displayed by Fig. 16 corresponds to a reduction of the Strouhal number, regardless of the sign of the acceleration. In particular, its maximum drop, around 8%, is observed in correspondence of the sixth reference wind speed $\overline{\overline{U}}_6$, when up-crossed, for an acceleration $< a >_W = 7.11\ \frac{m}{s^2}$. As concerns the ramp-down, the largest reduction is around 5%, and occurs when $\overline{\overline{U}}_7$ is down-crossed ($< a >_W =$ -5.11 $\frac{m}{s^2}$). Further commenting on the results of Fig. 16, it is clear that the maximum drop of the Strouhal number coincides with the largest absolute value of the acceleration. The same trend has been obtained by taking into consideration only 30 repeats of the test, indicating this number as sufficient for repeatability in the present test campaign. Therefore, an analogous analysis has been carried out for UF_6 as well, whose outcome shows minor discrepancies compared to the steady conditions. For this case, the maximum reductions in the Strouhal number are quantified as 4% for the ramp-up and 3% for the ramp-down.

Moving forward to the analysis of the effect of the acceleration on the harmonic content of $c_{\Delta P_L}$, the 90 wavelet power spectra gathered when U_W up-crosses $\overline{\overline{U}}_6$ for the ramp-up may be averaged, thus obtaining an ensemble mean of the instantaneous spectral content. This may be compared with the relevant steady reference (Section 3.2), evaluated in a consistent way. This comparison is reported in Fig. 17a which compares the two spectra drawn through solid lines: the steady one, defined by averaging the wavelet power spectra $P_{c_{\Delta P_L}}$ derived from the 90 repeats of UF_1, is in black, while the unsteady one is drawn in grey. A clear reduction of the shedding frequency is again observed. Moreover, the peak magnitude of the unsteady spectrum looks strongly reduced if compared to the steady one. Likewise, Fig. 17b reports the same plot concerning the down-crossing of $\overline{\overline{U}}_7$, which again points out the substantial reduction of the corresponding shedding frequency and of the spectrum. Analogous plots for all the 10 different reference velocities (for both ramp-up and ramp-down conditions) are shown in Brusco (2021).

The trends exhibited in Figs. 16 and 17a-b confirm again that the sign of the acceleration appears to play a central role in this phenomenon. Indeed, the frequency reductions seem to be more pronounced for the ramp-up, although it should be recalled that the positive accelerations are higher (in modulus) than the corresponding negative ones.

By taking the whole set of repeats into consideration, it is finally possible to evaluate the ensemble mean of the 90 ridges extracted from each repeat belonging to UF_1. The analysis of the ensemble mean of the ridges reveals a situation which apparently completely changes the findings of the single repeat. In fact, this curve entails a smooth transition from the different conditions, without any sort of discontinuity, as shown in Figs. 18a and b (for the ramp-up and the ramp-down conditions, respectively). These graphs again identify the temporal span of the transient conditions, in analogy with the analyses carried out on single repeats. The steady reference frequency values of the 10 up/down-crossed mean velocities are instead indicated through diamonds, whose presence points out that in both conditions the ridges are constantly lower than the frequencies evaluated by applying the Strouhal law, especially when the acceleration reaches its maximum or minimum, consistently with what reported in Figs. 16 and 17a-b. They are labelled as “QS” in the legend, recalling that they would correspond to the values of the instantaneous frequency should the ridge follow a quasi-steady variation. The absence of discontinuities in the average ridges of Figs. 18a-b confirms that the constant-frequency time cells and the associated discontinuities do not always occur exactly at the same values of velocity and acceleration. The same comment may be made by analyzing the mean of the energy maps, which again exhibits a clear and continuous ridge. Figs. 18a and b also report, through dash-dotted lines, the time instants for which the start and the end of ramp-ups and ramp-downs are considered (i.e., $< a >_W = \pm 0.25\ \frac{m}{s^2}$). Moreover, the steady reference frequencies linked to the initial and target wind velocity are also reported, being laid out in correspondence of the first and final instants, respectively.

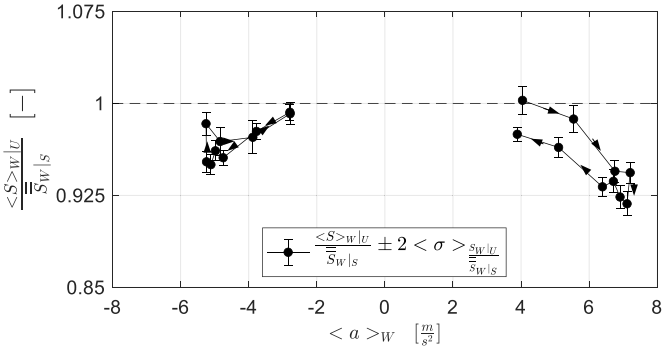

Fig. 16. Ensemble mean of the ratio between the Strouhal number in unsteady conditions (UF_1) and steady ones against $< a >_W$.

5. Conclusions and future perspectives

In this paper, the effects of free-stream acceleration and deceleration on the vortex-shedding from a sharp-edged square cylinder are studied experimentally in the multiple-fan wind tunnel of the Tamkang University. This facility is able to reproduce unsteady flows characterized by transients with accelerations of the order of those of real thunderstorm outflows. The experimental campaign is articulated in two different phases: the first concerns steady flows, whereas the second one deals with the simulation of unsteady conditions. The latter comprise the successive connection of two different velocities through transients with positive and negative acceleration. Particular attention has been given to two cases (denoted as UF_1 and UF_6), which differ because of the level of the achieved flow acceleration. The importance of the analysis of individual repeats is also emphasized in order to highlight types of

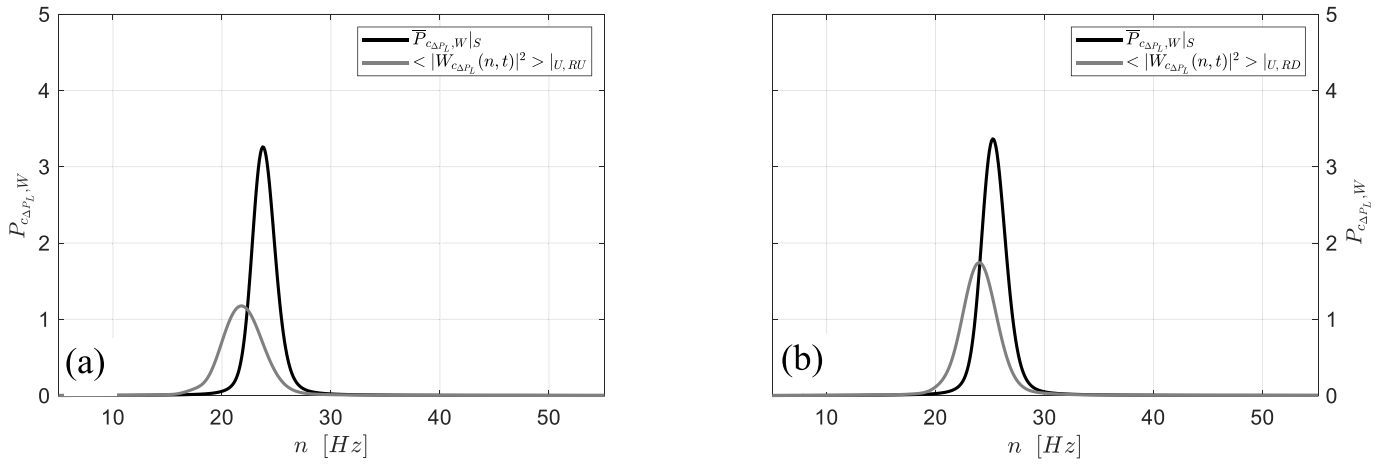

Fig. 17. Spectral comparison between unsteady and steady conditions for selected reference mean wind speed, taking 90 repeats of UF_1 into account: (a) ramp-up (RU), $< U >_W = \overline{\overline{U}}_6$; (b) ramp-down (RD), $< U >_W = \overline{\overline{U}}_7$.

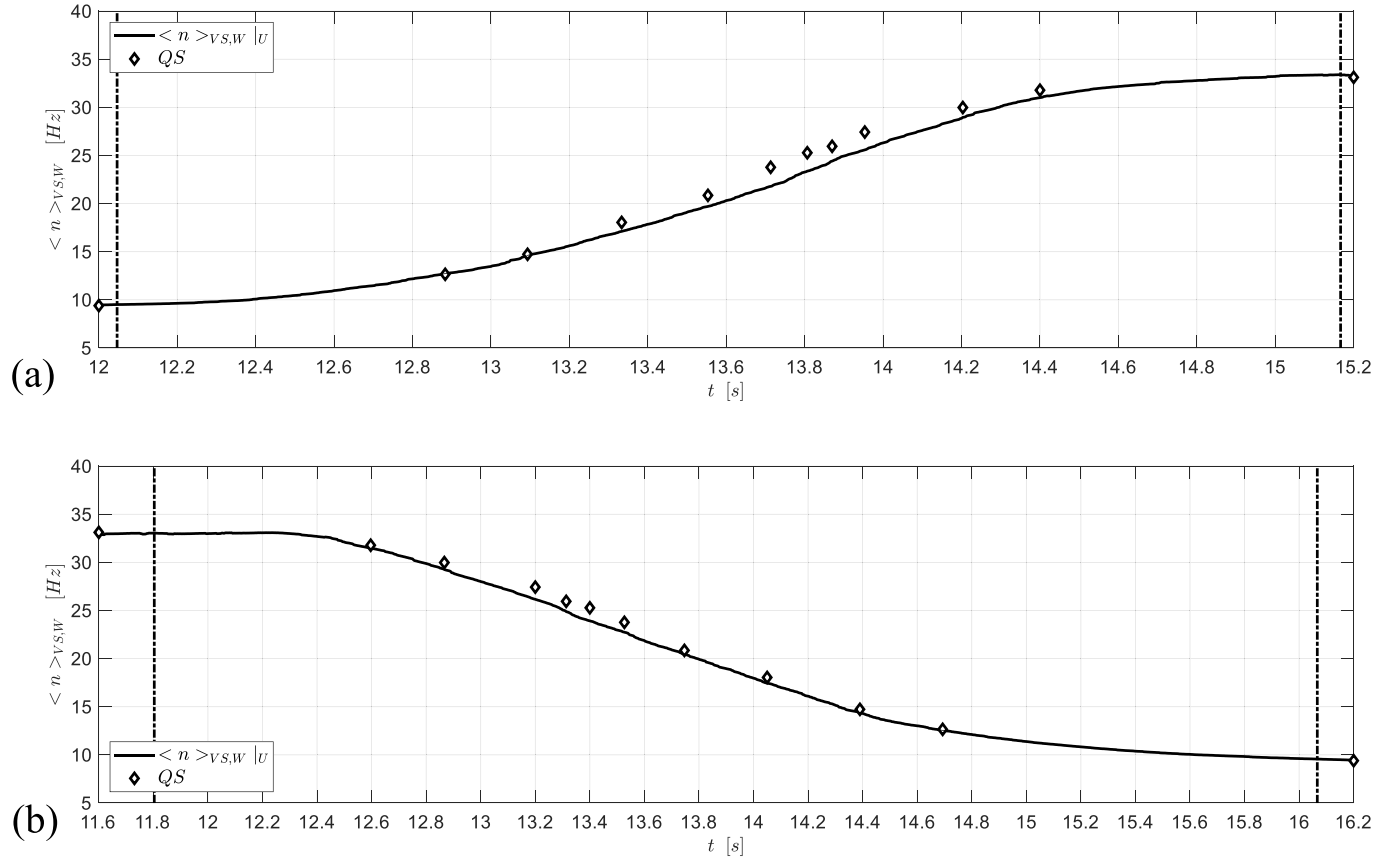

Fig. 18. Ensemble mean of the 90 ridges ($\omega_0 = 6\pi$) of $c_{\Delta P_L}$ for UF_1: (a) ramp-up; (b) ramp-down.

behavior that would be lost in an analysis of ensemble means.

In order to study the variation of the vortex-shedding frequency, both under steady and unsteady conditions, attention has been devoted to the non-dimensional cross-flow coefficient $c_{\Delta P_L}$, which is representative of the crosswind loading. Analyses for the unsteady flow cases have been carried out following several complementary paths. First, a visual inspection of $c_{\Delta P_L}$ from a single repeat of the unsteady flow UF_1 anticipates that in the transients the variation of the shedding frequency is not always regular. Time intervals characterized by a well-defined harmonic content are clearly present, together with parts of the signal in which the amplitude of the oscillations strongly drops. Secondly, tailored time-frequency analyses have been introduced, which are based on the continuous wavelet transform and on the Hilbert transform. Following a careful calibration of the time-frequency analysis procedures and a detailed scrutiny of the influence of the relevant parameters, the continuous wavelet transform with the Morlet wavelet and a central frequency $\omega_0 = 6\pi$ has been adopted.

The analysis of the whole set of data with these different methodologies clearly indicates the possible presence, in the transients, of time intervals characterized by a constant frequency, separated by

discontinuities. These constant-frequency time cells, which are more frequent and more pronounced in correspondence of higher absolute values of the acceleration, reflect a local violation of the theoretical Strouhal law and, to the best of the authors' knowledge, have not been previously described in the literature. Besides, the characteristics of the constant-frequency time cells apparently seem to be affected by the sign of the acceleration, probably because of a different dynamics of vortex-shedding in the wake. An analogy seems to exist between such discontinuities found in transient flows with those occurring along the axis of a two-dimensional slender structure immersed in a shear steady flow. While in the latter case their number and characteristics are ruled by a shear parameter, for accelerating flows they appear to be driven by the magnitude of the acceleration.

When analyzing the mean behavior of the variation of the shedding frequency, it is possible to observe that the shedding frequency at a certain instantaneous velocity appears to be similar to or definitely lower than its steady counterpart. This is particularly the case near absolute maximum values in acceleration, for both the ramp-up and ramp-down cases. As regards the peak magnitude of the wavelet power spectra in the transient flows, a remarkable reduction is also found compared to the steady conditions.

The above-described results suggest that the wake of the square cylinder and its features may be affected by the free-stream acceleration. Vortex-shedding appears to be weakened in its regularity, if compared to the steady case. Therefore, the configuration of the shed vortices is likely to be different, with peculiar features that are not yet clarified and whose characterization might be the objective of future investigations. On this respect, wind tunnel tests are quite challenging, as they require complex facilities and instrumentation. On the other hand, CFD techniques seem an appealing alternative choice (e.g., Guo et al., 2021). Indeed, numerical simulations might provide precious information about the effects of acceleration on the velocity and vorticity fields around the body. They could also be a valuable tool to estimate the wind-induced forces, since a deep knowledge of the wake and its features is necessary for the development of adequate procedures for the correct prediction of the aerodynamic loading on structures and structural elements in non-stationary flow conditions (e.g., Le and Caracoglia, 2015; Brusco et al., 2019; Brusco and Solari, 2021).

Dedication

The authors desire to dedicate this paper to the memory of Professor Giovanni Solari, whose profound passion for science and strong dedication to his students, as well as his genuine kindness, will always be an example and an inspiration for those who were lucky enough to meet him.

CRediT authorship contribution statement

Stefano Brusco: Conceptualization, Methodology, Data curation, Formal analysis, Investigation, Validation, Visualization, Writing – original draft. **Guido Buresti:** Conceptualization, Methodology, Software, Validation, Writing – review & editing, Supervision. **Yuan-Lung Lo:** Conceptualization, Writing – review & editing, Funding acquisition, Project administration. **Giuseppe Piccardo:** Conceptualization, Methodology, Writing – review & editing, Supervision, Funding acquisition, Project administration.

Declaration of competing interest

The authors declare that they have no known competing financial interests or personal relationships that could have appeared to influence the work reported in this paper.

Data availability

Data will be made available on request.

Acknowledgments

Stefano Brusco, Guido Buresti and Giuseppe Piccardo have been financially supported by the European Research Council under the European Union's Horizon 2020 research and innovation program (grant agreement No. 741273, Principal Investigator Professor Giovanni Solari) for the project THUNDERR - Detection, simulation, modelling and loading of thunderstorm outflows to design wind safer and cost-efficient structures – through an Advanced Grant 2016. The Authors thankfully acknowledge the support of the team of the Wind Engineering Research Center of the Tamkang University, for their time and help in performing the wind tunnel tests. In particular, the contribution of Mr. Hao-Yu Bin is greatly appreciated. Ms. Chia-Hua Wang, Ms. Giulia Adami and Mr. Davide Cosenza are greatly acknowledged for the rendering of the MFWT-TKU.

Appendix A. Supplementary data

Supplementary data to this article can be found online at https://doi.org/10.1016/j.jweia.2022.105182.

References

Akon, A.F., Kopp, G.A., 2018. Turbulence structure and similarity in the separated flow above a low building in the atmospheric boundary layer. J. Wind Eng. Ind. Aerod. 182, 87–100. https://doi.org/10.1016/j.jweia.2018.09.016.

Barlow, J.B., Rae, J.R., Pope A, W.H., 1999. Low-speed Wind Tunnel Testing. John Wiley & Sons. NY.

Bearman, P.W., Obasaju, E.D., 1982. An experimental study of pressure fluctuations on fixed and oscillating square-section cylinders. J. Fluid Mech. 119, 297–321. https://doi.org/10.1017/S0022112082001360.

Bearman, P.W., Trueman, D.M., 1972. An investigation of the flow around rectangular cylinders. Aeronaut. Q. 23 (3), 229–237. https://doi.org/10.1017/S0001925900006119.

Brusco, S., 2021. Transient Phenomena Induced by Thunderstorm Outflows on Slender Structures. PhD Thesis. University of Genoa. http://hdl.handle.net/11567/1051022.

Brusco, S., Solari, G., 2021. Transient aeroelasticity of structures subjected to thunderstorm outflows. Eng. Struct. 245, 112801 https://doi.org/10.1016/j.engstruct.2021.112801.

Brusco, S., Lerzo, V., Solari, G., 2019. Directional response of thunderstorm outflows. Meccanica 54, 1281–1306. https://doi.org/10.1007/s11012-019-00986-5.

Brusco, S., Buresti, G., Piccardo, G., 2022. Thunderstorm-induced mean wind velocities and accelerations through the continuous wavelet transform. J. Wind Eng. Ind. Aerod. 221, 104886 https://doi.org/10.1016/j.jweia.2021.104886.

Buresti, G., 1998. Vortex shedding from bluff bodies. In: "Wind Effects on Buildings and Structures" (Riera, J. D., Davenport, A. G., Eds.), Balkema, Rotterdam, pp. 61–95.

Buresti, G., 2012. Elements of Fluid Dynamics. Imperial College Press. London.

Buresti, G., Lombardi, G., Bellazzini, J., 2004. On the analysis of fluctuating velocity signals through methods based on the wavelet and Hilbert transforms. Chaos, Solit. Fractals 20, 149–158. https://doi.org/10.1016/S0960-0779(03)00438-7.

Canepa, F., Burlando, M., Solari, G., 2020. Vertical profile characteristics of thunderstorm outflows. J. Wind Eng. Ind. Aerod. 206, 104332 https://doi.org/10.1016/j.jweia.2020.104332.

Chay, M.T., Letchford, C.W., 2002. Pressure distributions on a cube in a simulated thunderstorm downburst. Part A: stationary downburst observations. J. Wind Eng. Ind. Aerod. 90 (7), 711–732. https://doi.org/10.1016/S0167-6105(02)00163-0.

Chen, J.M., Liu, C.H., 1999. Vortex shedding and surface pressures on a square cylinder at incidence to a uniform air stream. Int. J. Heat Fluid Flow 20 (6), 592–597. https://doi.org/10.1016/S0142-727X(99)00047-8.

Choi, E.C.C., 2000. Wind characteristics of tropical thunderstorms. J. Wind Eng. Ind. Aerod. 84 (2), 215–226. https://doi.org/10.1016/S0167-6105(99)00054-9.

De Gaetano, P., Repetto, M.P., Repetto, T., Solari, G., 2014. Separation and classification of extreme wind events from anemometric records. J. Wind Eng. Ind. Aerod. 126, 132–143. https://doi.org/10.1016/j.jweia.2014.01.006.

Durão, D.F.G., Heitor, M.V., Pereira, J.C.F., 1988. Measurement of turbulent and periodic flows around a square cross-section cylinder. Exp. Fluid 6, 298–304. https://doi.org/10.1007/BF00538820.

Dutta, S., Muralidhar, K., Panigrahi, P.K., 2003. Influence of the orientation of a square cylinder on the wake properties. Exp. Fluid 34 (1), 16–23. https://doi.org/10.1007/s00348-002-0484-x.

Gunter, W.S., Schroeder, J.L., 2015. High-resolution full-scale measurements of thunderstorm outflow winds. J. Wind Eng. Ind. Aerod. 138, 13–26. https://doi.org/10.1016/j.jweia.2014.12.005.

Guo, F., Wu, G., Du, X., Mason, M.S., 2021. Numerical investigation of flow around a square cylinder in accelerated flow. Phys. Fluids 33 (10), 104105. https://doi.org/10.1063/5.0062282.

Holmes, J.D., Hangan, H.M., Schroeder, J.L., Letchford, C.W., Orwig, K.D., 2008. A forensic study of the Lubbock-Reese downdraft of 2002. Wind Struct. 11, 19–39. https://doi.org/10.12989/was.2008.11.2.137.

Irwin, H.P.A.H., Cooper, K.R., Girard, R., 1979. Correction of distortion effects caused by tubing systems in measurements of fluctuating pressures. J. Wind Eng. Ind. Aerod. 5, 93–107. https://doi.org/10.1016/0167-6105(79)90026-6.

Kawai, H., 1983. Pressure fluctuations on square prisms – applicability of strip and quasi-steady theories. J. Wind Eng. Ind. Aerod. 13, 197–208. https://doi.org/10.1016/0167-6105(83)90141-1.

Kwan, K., Kopp, G.A., 2021. The effects of edge radius on wind tunnel tests of low-rise buildings. J. Wind Eng. Ind. Aerod. 214, 104668 https://doi.org/10.1016/j.jweia.2021.104668.

Le, T.H., Caracoglia, L., 2015. Reduced-order wavelet-Galerkin solution for the coupled, nonlinear stochastic response of slender buildings in transient winds. J. Sound Vib. 344, 179–208. https://doi.org/10.1016/j.jsv.2015.01.007.

Lee, B.E., 1975. The effect of turbulence on the surface pressure field of a square prism. J. Fluid Mech. 69 (2), 263–282. https://doi.org/10.1017/S0022112075001437.

Letchford, C.W., Chay, M.T., 2002. Pressure distributions on a cube in a simulated thunderstorm downburst. Part B: moving downburst observations. J. Wind Eng. Ind. Aerod. 90, 733–753. https://doi.org/10.1016/S0167-6105(02)00163-0.

Li, S., Snaiki, R., Wu, T., 2021. Active simulation of transient wind field in a multiple-fan wind tunnel via deep reinforcement learning. J. Eng. Mech. 147 (9), 04021056 https://doi.org/10.1061/(asce)em.1943-7889.0001967.

Lo, Y., Mason, M.S., 2019. Wind Loading of the CAARC Building during Velocity Profile Transitions, Part 2: Coherence of Transient Pressures. Proceedings of the 15th International Conference on Wind Engineering, pp. 831–832. Beijing, China.

Lombardo, F.T., Smith, D.A., Schroeder, J.L., Mehta, K.C., 2014. Thunderstorm characteristics of importance to wind engineering. J. Wind Eng. Ind. Aerod. 125, 121–132. https://doi.org/10.1016/j.jweia.2013.12.004.

Lyn, D.A., Rodi, W., 1994. The flapping shear layer formed by flow separation from the forward corner of a square cylinder. J. Fluid Mech. 267, 353–376. https://doi.org/10.1017/S0022112094001217.

Lyn, D.A., Einav, S., Rodi, W., Park, J.H., 1995. A laser-Doppler velocimetry study of ensemble-averaged characteristics of the turbulent near wake of a square cylinder. J. Fluid Mech. 304, 285–319. https://doi.org/10.1017/S0022112095004435.

Mair, W.A., Stansby, P.K., 1975. Vortex wakes of bluff cylinders in shear flow. SIAM J. Appl. Math. 28 (2), 519–540. https://doi.org/10.1137/0128040.

Mariotti, A., 2018. Axisymmetric bodies with fixed and free separation: base-pressure and near-wake fluctuations. J. Wind Eng. Ind. Aerod. 176, 21–31. https://doi.org/10.1016/j.jweia.2018.03.003.

Mariotti, A., Buresti, G., 2013. Experimental investigation on the influence of boundary layer thickness on the base pressure and near-wake flow features of an axisymmetric blunt-based body. Exp. Fluid 54 (11), 1612. https://doi.org/10.1007/s00348-013-1612-5.

Mariotti, A., Buresti, G., Gaggini, G., Salvetti, M.V., 2017. Separation control and drag reduction for boat-tailed axisymmetric bodies through contoured transverse grooves. J. Fluid Mech. 832, 514–549. https://doi.org/10.1017/jfm.2017.676.

Mason, M.S., Lo, Y., 2019. Wind Loading of the CAARC Building during Velocity Profile Transitions, Part 1: Transient Pressure Coefficient Distributions. Proceedings of the 15th International Conference on Wind Engineering, pp. 829–830. Beijing, China.

Mason, M.S., Letchford, C.W., James, D.L., 2005. Pulsed jet simulation of a stationary thunderstorm downburst. Part A: physical structure and flow field characterization. J. Wind Eng. Ind. Aerod. 93, 557–580. https://doi.org/10.1016/j.jweia.2005.05.006.

Maull, D.J., Young, R.A., 1973. Vortex shedding from bluff bodies in a shear flow. J. Fluid Mech. 60 (2), 401–409. https://doi.org/10.1017/S0022112073000236.

Mizota, T., Okajima, A., 1982. On the separated flow and variation of fluid force around a rectangular cylinder with section ratio 0.4 to 1.5 in a uniform flow. In: Proceedings of the 7th Symposium on Wind Engineering. Japan Association for Wind Engineering, Tokyo, pp. 75–81.

Morrison, M.J., Kopp, G.A., 2018. Effects of turbulence intensity and scale on surface pressure fluctuations on the roof of a low-rise building in the atmospheric boundary layer. J. Wind Eng. Ind. Aerod. 183, 140–151. https://doi.org/10.1016/j.jweia.2018.10.017.

Nakaguchi, H., Hashimoto, K., Muto, S., 1968. An experimental study on aerodynamic drag of rectangular cylinders. J. Jpn. Soc. Aeronaut. Eng. 16 (168), 1–5. https://doi.org/10.2322/jjsass1953.16.1.

Nakamura, Y., Ohya, Y., 1984. The effects of turbulence on the mean flow past two-dimensional rectangular cylinders. J. Fluid Mech. 149 (1), 255–273. https://doi.org/10.1017/S0022112084002640.

Noda, H., Nakayama, A., 2003. Free-stream turbulence effects on the instantaneous pressure and forces on cylinders of rectangular cross section. Exp. Fluid 34 (3), 332–344. https://doi.org/10.1007/s00348-002-0562-0.

Norberg, C., 1993. Flow around rectangular cylinders: pressure forces and wake frequencies. J. Wind Eng. Ind. Aerod. 49 (1–3), 187–196. https://doi.org/10.1016/0167-6105(93)90014-F.

Obasaju, E.D., 1983. Investigation of the effects of incidence on the flow around a square section cylinder. Aeronaut. Q. 34 (4), 243–259. https://doi.org/10.1017/S0001925900009768.

Okajima, A., 1982. Strouhal numbers of rectangular cylinders. J. Fluid Mech. 123, 379–398. https://doi.org/10.1017/S0022112082003115.

Okajima, A., Nagahisa, T., Rokugoh, A., 1990. A numerical analysis of flow around rectangular cylinders. JSME Int. J. Ser. II 33, 702–711. https://doi.org/10.1299/jsmeb1988.33.4_702.

Ootsuki, S., Fujii, K., Washizu, H., Ohya, S., 1980. On the characteristics of three component aerodynamic force and pressure distribution of a fixed two-dimensional rectangular cylinder in a uniform flow. In: Proceedings of the 6th Symposium on Wind Engineering, Japan Association for Wind Engineering, Tokyo, pp. 153–159.

Ozono, S., Ikeda, H., 2018. Realization of both high-intensity and large-scale turbulence using a multi-fan wind tunnel. Exp. Fluid 59, 187. https://doi.org/10.1007/s00348-018-2647-4.

Petty, D.G., 1979. The effect of turbulence intensity and scale on the flow past square prisms. J. Wind Eng. Ind. Aerod. 4 (3–4), 247–252. https://doi.org/10.1016/0167-6105(79)90005-9.

Roberson, J.A., Lin, C.Y., Rutherford, G.S., Stine, M.D., 1972. Turbulence effects on drag of sharp-edged bodies. J. Hydraul. Div. ASCE 98 (HY7), 1187–1203. https://doi.org/10.1061/JYCEAJ.0003350.

Saathoff, P.J., Melbourne, W.H., 1997. Effects of free-stream turbulence on surface pressure fluctuations in a separation bubble. J. Fluid Mech. 337, 1–24. https://doi.org/10.1017/S0022112096004594.

Sarpkaya, T., 1963. Lift, drag, and mass coefficients for a circular cylinder immersed in time ependent flow. J. Appl. Mech. 30, 13–15. https://doi.org/10.1115/1.3630062.

Sarpkaya, T., 1966. Separated flow about lifting bodies and impulsive flow about cylinders. AIAA J. 414–420. https://doi.org/10.2514/3.3453.

Sarpkaya, T., Ihrig, C., 1986. Impulsively started steady flow about rectangular prisms: experiments and discrete vortex analysis. J. Fluid Eng. 108, 47–54. https://doi.org/10.1115/1.3242542.

Sarpkaya, T., Kline, H., 1982. Impulsively-started flow about four types of bluff body. J. Fluid Eng. 104, 207–213. https://doi.org/10.1115/1.3241809.

Shirato, H., Maeta, K., Kato, Y., Takasugi, Y., 2009. Transient drag force on 2-d bluff bodies under gusty wind condition. In: Proceedings of the 7th Asia-Pacific Conference on Wind Engineering. Taipei, Taiwan.

Sohankar, A., 2006. Flow over a bluff body from moderate to high Reynolds numbers using large eddy simulation. Comput. Fluids 35 (10), 1154–1168. https://doi.org/10.1016/j.compfluid.2005.05.007.

Solari, G., 1985. Mathematical model to predict 3-D wind loading on buildings. J. Eng. Mech. 111 (2), 254–276. https://doi.org/10.1061/ASCE)0733-9399(1985)111:2(254).

Solari, G., 2014. Emerging issues and new frameworks for wind loading on structures in mixed climates. Wind Struct. 19, 295–320. https://doi.org/10.12989/was.2014.19.3.295.

Solari, G., 2019. Wind Science and Engineering. Springer Nature Switzerland.

Solari, G., 2020. Thunderstorm downburst and wind loading of structures: progress and prospect. Front. Built. Environ. 6 (63), 1–24. https://doi.org/10.3389/fbuil.2020.00063.

Solari, G., Burlando, M., Repetto, M.P., 2020. Detection, simulation, modelling and loading of thunderstorm outflows to design wind-safer and cost-efficient structures. J. Wind Eng. Ind. Aerod. 200, 104142 https://doi.org/10.1016/j.jweia.2020.104142.

Takeuchi, T., Maeda, J., 2013. Unsteady wind force on an elliptic cylinder subjected to a short-rise-time gust from steady flow. J. Wind Eng. Ind. Aerod. 122, 138–145. https://doi.org/10.1016/j.jweia.2013.06.008.

Takeuchi, T., Maeda, J., Kawashita, H., 2008. The overshoot of aerodynamic forces on a railcar-like body under step-function-like gusty winds. In: Proceedings of the 6th International Colloquium on Bluff Body Aerodynamics and Applications Milano, Italy.

Tamura, T., Miyagi, T., 1999. The effect of turbulence on aerodynamic forces on a square cylinder with various corner shapes. J. Wind Eng. Ind. Aerod. 83 (1–3), 135–145. https://doi.org/10.1016/S0167-6105(99)00067-7.

Vickery, B.J., 1966. Fluctuating lift and drag on a long cylinder of square cross-section in a smooth and in a turbulent stream. J. Fluid Mech. 25 (3), 481–494. https://doi.org/10.1017/S002211206600020X.

Vickery, B.J., Clark, A.W., 1972. Lift or across-wind response of tapered stacks. J. Struct. Div. ASCE 98 (1), 1–20. https://doi.org/10.1061/JSDEAG.0003103.

Xhelaj, A., Burlando, M., Solari, G., 2020. A general-purpose analytical model for reconstructing the thunderstorm outflows of travelling downbursts immersed in ABL flows. J. Wind Eng. Ind. Aerod. 207, 104373 https://doi.org/10.1016/j.jweia.2020.104373.

Yang, T., Mason, M.S., 2019. Aerodynamic characteristics of rectangular cylinders in steady and accelerating wind flow. J. Fluid Struct. 90, 246–262. https://doi.org/10.1016/j.jfluidstructs.2019.07.004.